MEASURING OPTICAL ABSORPTION COEFFICIENT OF PURE WATER IN UV USING THE INTEGRATING CAVITY ABSORPTION METER

A Dissertation

by

LING WANG

Submitted to the Office of Graduate Studies of
Texas A&M University
in partial fulfillment of the requirements for the degree of

DOCTOR OF PHILOSOPHY

May 2008

Major Subject: Physics

MEASURING OPTICAL ABSORPTION COEFFICIENT OF PURE WATER IN UV USING THE INTEGRATING CAVITY ABSORPTION METER

A Dissertation

by

LING WANG

Submitted to the Office of Graduate Studies of
Texas A&M University
in partial fulfillment of the requirements for the degree of

DOCTOR OF PHILOSOPHY

Approved by:

Chair of Committee,	Edward S. Fry
Committee Members,	Robert A. Kenefick
	Alexei Sokolov
	Goong Chen
Head of Department,	Edward S. Fry

May 2008

Major Subject: Physics

ABSTRACT

Measuring Optical Absorption Coefficient of Pure Water in UV Using
the Integrating Cavity Absorption Meter. (May 2008)

Ling Wang, B.S., Peking University, P. R. China;
M.S., Peking University, P. R. China
Chair of Advisory Committee: Dr. Edward S. Fry

The integrating cavity absorption meter (ICAM) has been used successfully to measure the low absorption coefficient of pure water. The ICAM produces an effective total path length of several meters or even longer, although the physical size of the instrument is only several centimeters. The long effective total path length ensures a high sensitivity that enables the ICAM to measure liquid mediums with low absorption. Compared to the conventional transmission type of instruments that were used to measure the same medium with the same path length, the ICAM eliminates the effect of scattering by introducing isotropic illumination in the medium, and consequently measures the true absorption coefficient of the medium in stead of the attenuation coefficient. The original ICAM was constructed with Spectralon and used in the wavelength range from 380 nm to 700 nm. Later studies showed that Spectralon is not suitable for measurements in the UV region because of its relatively lower reflectivity in this region and, even worse, the continuously decaying reflectivity under the exposure to UV radiation. Thus, we have developed a new way to construct the ICAM utilizing the material fumed silica. The resulting ICAM has a high sensitivity even in the UV region and doesn’t have the deterioration problem. The measurement results from the new ICAM are in good agreement with the existing results. The absorption coefficients of pure water at wavelengths between 250 nm and 400 nm are presented here.

To My Parents

ACKNOWLEDGEMENTS

I would like to thank my committee chair, Dr. Fry, and my committee members, Dr. Kenefick, Dr. Sokolov, and Dr. Chen, for their guidance and support throughout the course of this research.

Thanks also go to my friends and colleagues for making my time at Texas A&M University a great experience. The discussions with Dr. Cechan Tian, Dr. Gangyao Xiao, Dr. Hongxing Meng, Dr. Joseph Musser and Jeffrey Katz were helpful and led to the success of my research. I also want to extend my gratitude to the Robert A. Welch Foundation, which supported my research, and to the machine shop and electronic shop in the physics department and the glass shop in the chemistry department for sharing their expertise unselfishly.

Finally, thanks to my mother and father for their encouragement and to my wife for her love and extreme patience. And special thanks to my daughter, who brought sunshine even in my worst days.

TABLE OF CONTENTS

LIST OF FIGURES

FIGURE Page

LIST OF TABLES

CHAPTER I

INTRODUCTION

Water is one of the most important molecules on Earth, which makes our planet different from other known celestial bodies. Water covers about 70% of the surface of Earth, mostly as saltwater in the ocean (97%). Some is fresh water in rivers and lakes; some is in the form of ice or vapor. In the ocean, phytoplankton are at the bottom of the food chain; they play the same role as vegetation on land. They obtain energy from the Sun's electromagnetic radiation, and through the process of photosynthesis, they provide the initial step in the food chain for all life in the oceans. Consider one of these remarkable food chains in the ocean: some of the largest organisms on Earth, whales, feed on krill, which in turn feed on phytoplankton, the smallest organisms on Earth. Phytoplankton are also responsible for making up to 90% of Earth's oxygen. Radiation originates from the Sun, passes through space and the atmosphere of the Earth, penetrates the ocean, and reaches the phytoplankton. To understand the ecosystems of the ocean, it is important to understand how the atmosphere and water affect the Sun's radiation, i.e. how radiation is absorbed and scattered.

The spectrum of the sun's radiation is close to that of a black body at a temperature of 5800 K, visible (VIS) light is just a small part of it. Ultraviolet radiation (UVR) is that

---

This dissertation follows the style of Applied Optics.

part of the spectrum with a wavelength less than 400 nm. UVR has been recognized as a potential stress for organisms in a variety of environments, including the marine ecosystems [1, 2]. Fortunately, stratospheric ozone absorbs most of the UVR and protects the environment from the detrimental UV-B (280 nm-320 nm) radiation. But recent studies showing an intensifying anthropogenic-induced decline in stratospheric ozone concentrations with concurrent enhanced UV-B radiation are alarming. This alteration of the sun's radiation spectrum on the earth's surface poses some potential problems for the established balances in the marine ecosystems. The resulting changes are the subject of many ongoing multidisciplinary studies including physics, chemistry and biology. Since the knowledge of the distribution of UVR in the ocean is fundamental, the optical properties of water in the UV range are very important subjects of research.

1. Optical properties of water

The water molecule is one of the simpler molecules in the universe, composed of only three atoms: one oxygen atom and two hydrogen atoms (Fig. 1.1) [3].

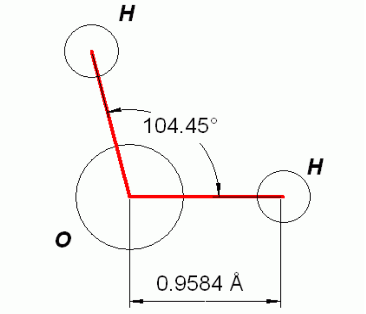

Fig. 1.1. Water molecule.

However, the energy structure of the water molecule is complex. Because of its importance, the high resolution energy structure of the water molecule has been under decades of intense studies. In reference [4], Tennyson et al. have tabulated 12248 vibration–rotation states of the water molecule. Researchers are still working to expand the table and approach the full set of the states [5, 6].

The water molecule is under constant vibrational and rotational motions. Fig. 1.2 shows the fundamental vibration and rotation modes of the water molecule [7]. In gaseous water, the frequency of the symmetric stretch mode (ν_1) is 3657.05 cm^{-1} (2.73444 μm). The frequency of the asymmetric stretch mode (ν_3) is 3755.93 cm^{-1} (2.66246 μm). And that of the bend mode (ν_2) is 1594.75 cm^{-1} (6.27058 μm). The water molecule has a small moment of inertia on rotation which gives rise to rich combined vibrational-rotational spectra in the vapor containing millions of absorption lines. In the liquid, rotations tend to be restricted by hydrogen bonding, giving the librations. Also, the spectral lines are broadened, resulting in an overlap of many of the absorption lines.

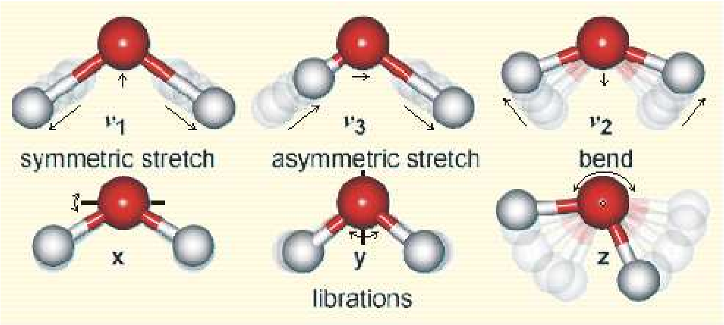

Fig. 1.2. Vibration and rotation modes of water molecule.

The absorption spectrum of liquid water has been intensively studied. Its structure is very complicated and is still a topic of current research. Since its molecules are connected by hydrogen bonds, the structure of liquid water gives rise to several anomalies when compared to other liquids. Fig. 1.3 shows a combination of data on the absorption coefficient of the liquid water for electromagnetic radiation at wavelengths from 40 nm to 1 mm [7, 8]. The absorption coefficient $a(\lambda)$, with unit m^{-1}, at a particular wavelength is defined as in $I/I_0=\exp(-a(\lambda)L)$, where I is the transmitted intensity of the light, I_0 is the incident intensity of the light and L is the path length (m). (Sometimes the absorption coefficient $a(\lambda)$ is given in unit cm^{-1}, with 1 cm^{-1} equal to 100 m^{-1}.) In this dissertation, most of the time I will only write a for $a(\lambda)$, but a is always wavelength dependent.

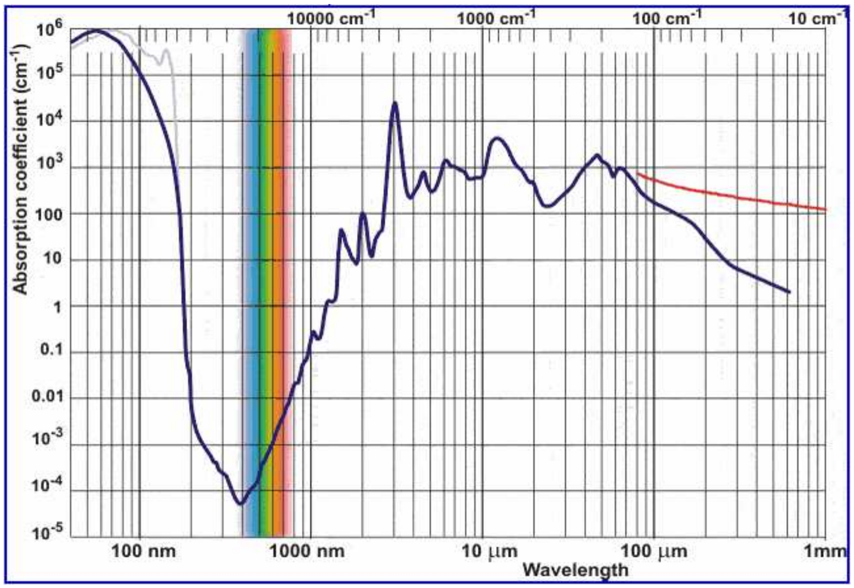

Fig. 1.3. Absorption coefficient of water.

In Fig. 1.3, the blue line is the absorption coefficient of water. The light blue line shows some spectrum structure only existent in gaseous water. The red line shows some different values for the 80μm to 1mm region. This data is compiled from the existing literatures. Some part of the data, e.g. data in the UV region, is arguable and must be verified by independent investigations. Our present research objective is to measure the absorption coefficient of pure water in the UV region and clarify the confusion.

For ocean color studies, the spectral absorption of water provides vital input into the modeling of spectral reflectance [9]. Of equal importance is another optical property of water: scattering. Scattering in water is discussed in detail by Morel [10]. The following relations and definitions are used:

$$c = a + b, \tag{1.1}$$

$$b = \iint_{4\pi} \beta(\theta) d\Omega = 2\pi \int_0^{\pi} \beta(\theta) \sin\theta d\theta, \tag{1.2}$$

where c is the attenuation coefficient, a the absorption coefficient, b the total scattering coefficient and $\beta(\theta)$ the volume scattering function. Attenuation, absorption and scattering are all wavelength dependent.

Absorption and scattering characteristics are inherent optical properties (IOP) of water. They only depend on the water through which the light is propagating, not on the nature of the light field itself. Properties that are directly derived from the light field are called apparent optical properties (AOP). Changing the light field that enters the water body, for example by a cloud moving in front of the sun immediately changes the AOP, but not the IOP. If one knows all of the IOPs of a water body and the light field above the surface, one can, in principle, calculate the light field anywhere in the water body. On the other hand, it is possible to estimate the IOPs of water body from measurements of the AOPs. This is the so called inverse problem of hydrologic optics. From the IOPs, it is possible to extract information about suspended and dissolved substances in the water body.

Natural waters can be of great purity, e.g. deep sea waters. Consequently, pure water itself plays an important part in absorption and scattering processes. Natural waters have dissolved organic or inorganic materials as well as suspended particles. These materials have their own characteristic absorption and scattering properties. Pure water IOPs provide a baseline for studies of diffuse attenuation coefficients in water as well as the absorption by dissolved or suspended organic and biological materials.

2. Measurement methods

Because of its importance, the optical absorption of pure water has been of interest to many researchers. Accordingly, various techniques to measure absorption have been developed. Querry et. al. give an extensive review of research on the spectral absorption coefficient for pure water [11]. Here we briefly review some of the techniques that have been used for absorption in the visible and UV regions.

The most intuitive technique to measure absorption of water is the conventional transmission type measurement. Hulburt et. al. used a long path length tube of distilled pure water to measure the attenuation of a beam of light; they then mathematically corrected for the scattering losses using measured or calculated scattering coefficients [12, 13]. Other researchers have also made measurements using similar techniques [14-19]. The obvious problem of the transmission type measurement is that the measured quantity is actually attenuation, not absorption, coefficient. Usually, the scattering coefficient is calculated and equation 1.1 is used to get the absorption coefficient. There are also other problems. To measure the low absorption of pure water, the path length must be long, sometimes several meters. Long path lengths pose problems in making large amounts of pure water; they complicate optical alignment, and they significantly increased the errors associated with the scattering corrections. Usually, the pure water samples are sealed in tubes. The interfaces of each window with air and water produce reflection and scattering. These effects must also be carefully compensated; otherwise, the error could easily be as large as the absorption itself.

At the same time, some ingenious true absorption techniques were also developed. Hass et. al. used a collimated high power continuous wave (cw) laser beam to illuminate a pure water sample and monitored the temperature change of the water [20, 21]. Stone used photothermal techniques based on the temperature dependence of the index of refraction [22], while Tam and Patel used photoacoustic techniques [23-25]. They sent a pulsed laser beam through a cell filled with water, and then monitored the acoustic wave caused by the heating of water by the laser pulses. Sogandares and Fry measured the absorption spectrum of the purest available water with photothermal deflection spectroscopy [26].

Because the optical absorption of water in the visible and UV regions is very low (less than 0.01 m^{-1} at its minimum), accurate measurements are difficult. Careful examination of measurement results shows the inconsistencies in the data. Differences by an order of magnitude at the same wavelength are not uncommon. The inconsistencies are probably due to a combination of both experimental error and unknown sample purity. Pope and Fry’s measurement of absorption from 380 nm to 700 nm using their integrating cavity absorption meter (ICAM) [27, 28] have cleared up much of the confusion. . Their data is highly reliable due to many crosschecks and consistency tests. It is in excellent agreement with recent measurements of absorption coefficients for deep sea ice [29] and with those obtained by Sogandares and Fry. The importance of the data has been emphasized by Morel: “…Such a drastic revision is of considerable impact, in particular on the understanding of the optical properties of extremely pure oligotrophic, waters, which form a wide part of the world ocean. These new values, in the violet part of the spectrum, strongly suggest that the currently admitted absorption coefficients in the near-UV (400 - 300 nm) domain are likely to be also revised.” [9]

3. ICAM

Due to the extremely successful performance of the ICAM in the visible and near UV parts of the spectrum, we are modifying the design for operational wavelengths in the deeper UV region.

Integrating cavity spectroscopy was first introduced by Elterman for materials with small absorption coefficient [30]. The advantage of this method was stated as “being independent of the scattering within the material sample, the reflectivity of the material surface, and the geometry of the sample”. Later the technique was adopted and refined by Fry et. al. to measure the small absorption coefficient of a liquid sample, particularly, pure water [27]. The idea is very simple, as shown in Fig. 1.4.

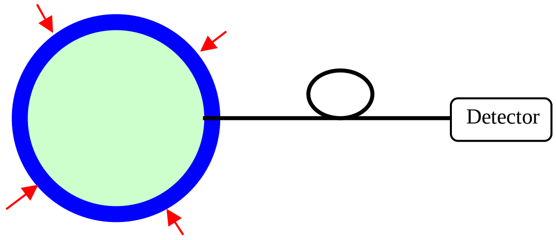

Fig. 1.4. ICAM simplified. (Cross section)

Consider a spherical integrating cavity (the blue shell in Fig. 1.4.) that’s uniformly illuminated by monochromatic light from outside. The wall of the cavity is made of translucent material with highly diffuse, highly reflective surface. Light leaks through the wall, reflects off the surface of cavity wall many times and builds up a uniform light field. The inside of the integrating cavity can be either empty or filled with liquid sample. When the cavity is filled with a medium, some light is absorbed by the medium. Thus energy is lost from the radiation field and transferred to heat. This loss results in a reduction of the outward irradiance at the inner surface of the cavity. A fiber is used to sample this outward irradiance. By comparing the outward irradiance from both an empty cavity and a full cavity, it is possible to calculate the absorption coefficient of the liquid sample.

The advantages of the ICAM are twofold. First, photons undergo many internal reflections in the cavity before they are lost, either by absorption in the sample or transmission through the wall. The effective path length is consequently very long (many times larger than the physical size of the cavity itself), making it suitable for the measurement of a low absorption medium, e.g. pure water. Second, since the light field in the cavity is already isotropic, it cannot be made more isotropic by scattering within the medium. Therefore, the measurement is insensitive to scattering effects.

The objective of our research is to modify the ICAM to measure water absorption in the near UV region. That involves considerable changes of the original design, as discussed in the following chapters.

CHAPTER II

THEORETICAL BACKGROUND

1. Theory

In order to provide uniform illumination of the sample in a spherical ICAM, the integrating cavity shown in Fig. 1.4 is put inside of another larger spherical integrating cavity, as shown in Fig. 2.1.

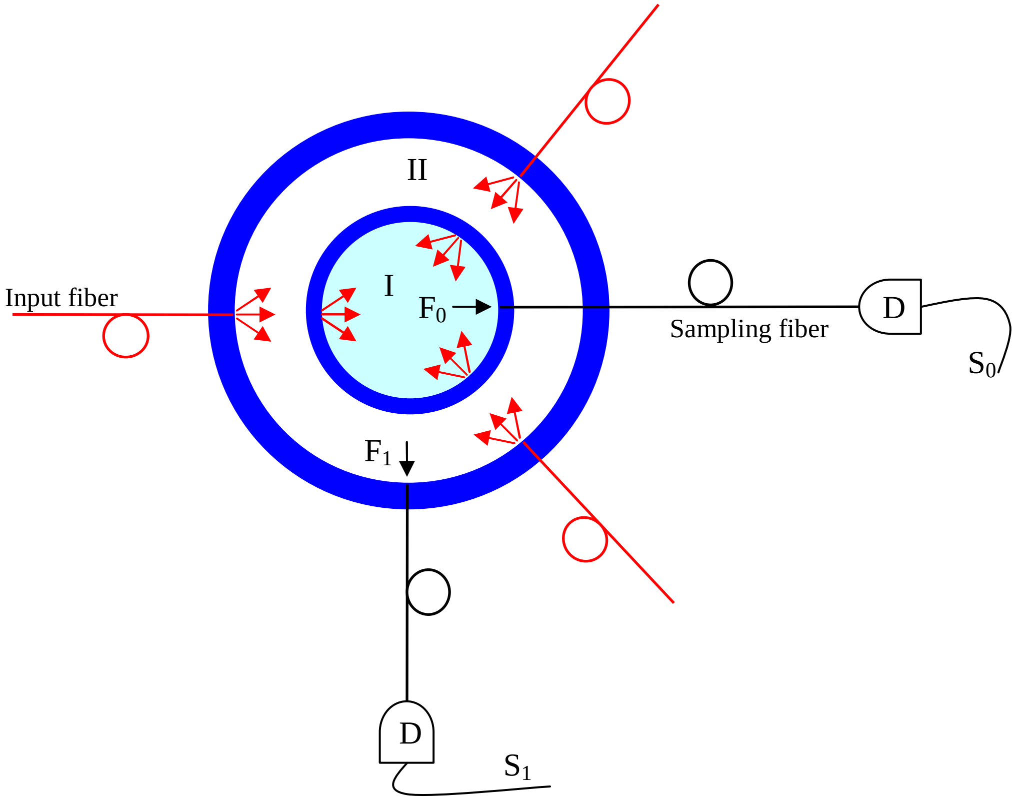

Fig. 2.1. Cross section of a generic model of ICAM.

Both of the integrating cavities are made of material with highly diffuse reflective surfaces. High reflectivity usually means over 99% reflectivity (it depends on the wavelength). Ideally diffuse means a Lambertian surface. Cavity I is formed by the inside of the smaller sphere. Cavity II is formed by the outer surface of the smaller sphere and inner surface of the larger sphere. Monochromatic light is introduced into cavity II by means of input fibers. Light reflects off the surfaces of cavity II many times and builds up a uniform light field. Some light leaks through the smaller cavity wall and builds up a uniform isotropic field in cavity I. The inherently anisotropic introduction of radiation into cavity II is converted into a nearly isotropic illumination of a sample placed in cavity I. It should be noted that although the wall of cavity I has high reflectivity, the light is incident many times until an appreciable fraction gets through the wall into cavity I. Ideally, the energy density in cavity I should be the same as that in cavity II if there were no losses in cavity I other than the transmission loss through the wall. Two optical fibers are used to sample the outward irradiances from cavity I and cavity II, respectively. Light is carried by the fibers to detectors, which produce signals S_0 and S_1, proportional to the outward irradiances F_0 and F_1 in cavity I and cavity II, respectively.

The theory of this generic model of ICAM has been developed by Fry et. al. [27, 28]. Let the scalar $L(\mathbf{r}, \Omega)$ denote the radiance in the direction of unit vector Ω at point $\boldsymbol{r}$. Then, at point $\boldsymbol{r}$, we can define a vector irradiance $\boldsymbol{F}$:

$$F = \int_{\Omega} L(r,\Omega)\hat{\Omega}d\Omega \tag{2.1}$$

and a radiant energy density U:

$$U = \frac{m}{c}\int_{\Omega} L(r,\Omega)d\Omega \qquad (2.2)$$

where the integral is over solid angle *Ω*, *c* is the speed of light in vacuum, and *m* is the refractive index of the homogeneous medium in the cavity [31]. Starting from equations of radiative transfer [32], we have:

$$\hat{\Omega}\cdot\nabla L(r,\Omega) = -\beta_e L(r,\Omega) + \frac{\beta_s}{4\pi}\int_{\Omega'} p(\Omega,\Omega')L(r,\Omega')d\Omega' \qquad (2.3)$$

where β_e is the attenuation coefficient (we choose this instead of *c* as defined before to avoid the confusion with speed of light), β_s is the scattering coefficient, and *p* is the scattering phase function. The equation is easy to understand: the change of the radiance along one specific direction is due to the loss from the attenuation effect and the gain from scattering of the radiance in other directions. The scattering phase function *p* satisfies the normalization equation:

$$\frac{1}{4\pi}\int_{\Omega} p(\Omega,\Omega')d\Omega = 1 \qquad (2.4)$$

Integrating equation 2.3 over solid angle Ω, it's straightforward to get

$$-\nabla\cdot F = \frac{ac}{m}U \qquad (2.5)$$

In the above equation, we have replaced (β_e- β_s) with *a*, the absorption coefficient, by definition of equation 1.1. This fundamental relation is valid in every point in the medium, irrespective of the magnitude of any scattering effect.

Integrating equation 2.5 over volume *V* of the sample and using divergence theorem on the left hand side, we find

$$-\int_{s} F \cdot dS = \frac{ac}{m}\int_{V} U dV \qquad (2.6)$$

The left hand side of equation 2.6 is the net radiant power entering the sample volume, i.e. it is the power P that is absorbed in the sample. Thus we have

$$P_{abs} = \frac{ac}{m}\int_{V} U dV \qquad (2.7)$$

For a homogeneous medium this result is exact and is rigorously independent of any scattering effect. If the energy density is also homogeneous (i.e. constant), we can simply integrate the right side of equation 2.7 to obtain

$$P_{abs} = \frac{ac}{m} UV \qquad (2.8)$$

A form of more practical use is obtained by relating the energy density *U* inside the sample to the normal component of ***F*** at the inside surface of the sample. This normal component F_{out} is just the outwardly directed irradiance at the surface of the sample. If the radiance distribution in the sample is both homogeneous and isotropic, then $L(\mathbf{r},\Omega)$ is a constant. Equations 2.1 and 2.2 then become, respectively,

$$F_{out} = \hat{n} \cdot \int_{\Omega} L(r,\Omega)\hat{\Omega} d\Omega = \pi L\,, \qquad (2.9)$$

$$U = \frac{4\pi m}{c} L\,, \qquad (2.10)$$

where ***n*** is the outward unit vector normal to the surface. These two equations give the relation between F_{out} and *U*,

$$U = \frac{4m}{c} F_{out} \qquad (2.11)$$

Thus the final result for the absorbed power is

$$P_{abs} = 4aVF_{out} \tag{2.12}$$

In the ICAM, irradiance relationships can be obtained by using the law of energy conservation within each cavity; specifically, the total power entering cavity I is equal to the total power leaving the cavity plus the power absorbed in it,

$$P_{in} = P_{out} + P_{abs} = P_{out} + 4aVF_0 \, , \tag{2.13}$$

where we have used equation 2.12 and replaced F_{out} with F_0, the outward irradiance in cavity I. We will assume that the radiance at any point in cavity I is isotropic and homogeneous, and the radiance at any point in cavity II is proportional to the radiance at other points in the same cavity, as the result of the cavity configuration. The radiance is actually nearly uniform and isotropic in each cavity, but it is only required in cavity I.

We can write the power in and power out in terms of irradiances, F_0 and F_1. The power entering cavity I will be proportional to F_1. The power leaving the cavity through the wall and sampling fiber will be proportional to F_0. The power conservation equation can be written as

$$K_1F_1 = K_0F_0 + 4aVF_0 \, , \tag{2.14}$$

where K_0 and K_1 are proportionality constants. As described before, the irradiances are sampled by the sampling fibers and sent to detectors to produce corresponding signal voltages S_0 and S_1. Since these voltages depend on the spectral response of the detectors and the fiber optics, equation 2.14 can be rewritten as

$$C_1S_1 = C_0S_0 + 4aVS_0 \, , \tag{2.15}$$

where C_0 and C_1 are new set of proportionality constants. C_0 and C_1 are wavelength dependent and cavity configuration dependent. Dividing equation 2.15 by C_1S_0 and replacing S_1/S_0 by S gives a simpler equation that is linear in S, a and V:

$$S = \frac{4}{C_1} aV + C_0^{'} , \tag{2.16}$$

where we have also replaced C_0/C_1 by $C_0^{'}$. The partial derivative of S with respect to V will be used later to determine the absorption coefficient of pure water:

$$\left.\frac{\partial S}{\partial V}\right|_a = \frac{4}{C_1} a . \tag{2.17}$$

If we have a sample, e.g. a dye solution, whose absorption coefficient is already known, we can fill the cavity with this sample gradually. For each volume, we measure the signals S_0 and S_1 and calculate the quantity S. Then we plot S versus volume V and determine the slope, $(\partial S/\partial V)_{sample}$. From the slope we calculate the calibration constant C_1 using equation 2.17. Next, we fill the cavity gradually with pure water, do the same procedure again and determine $(\partial S/\partial V)_{purewater}$ for pure water. We can use this two slopes information to determine the absorption coefficient of pure water. It should be noted that $\partial S/\partial V$, C_1 and a are all wavelength dependent. During the measurement, light from a monochromator is used for illumination and data are recorded at regular wavelength intervals.

2. Photon behavior in ICAM

From the analysis above, we see clearly that scattering has no effect on the measurement of the absorption coefficient. The reason is that the light field is already uniform and isotropic in the cavity and scattering cannot make it more or less isotropic. The other advantage of the ICAM is the very long effective path length (compared to the physical size of the apparatus itself). It is easily understood because light reflects off the highly reflective wall many times before it escapes from the cavity. By examining the photon behavior, we can get an analytical result for the effective path length in a spherical integrating cavity [33].

Consider a population of photons emitted into an empty cavity with wall reflectivity of ρ. Every time a photon has a collision with the wall, the probability it survivs the collision and stays in the cavity is ρ. The probability that the photon transmits through the wall or is absorbed by the wall is (1- ρ). The average lifetime of each photon staying in the cavity can be measured in terms of the number of collisions it undergoes in the cavity. For the whole population of photons, we define P_1 as the proportion that has one collision, P_2 as the proportion that has two collisions and so on. The proportion that has survived (n-1) collisions is ρ^{n-1}, of which (1- ρ) is lost in the next, i.e. nth, collision. Thus the proportion that has exactly n collisions is given as:

$$P_n = \rho^{n-1}(1-\rho)\ . \tag{2.18}$$

The average number C_E of collisions for a photon is

$$\begin{aligned} C_E &= P_1 \cdot 1 + P_2 \cdot 2 + P_3 \cdot 3 + ... + P_n \cdot n + ... \\ &= (1-\rho) + \rho(1-\rho) \cdot 2 + \rho^2(1-\rho) \cdot 3 + ... + \rho^{n-1}(1-\rho) \cdot n + ... \\ &= (1-\rho)(1 + 2\rho + 3\rho^2 + ... + n\rho^{n-1} + ...) \\ &= \frac{1}{1-\rho} \end{aligned} \tag{2.19}$$

This result doesn't depend on the shape of the cavity. The effective total path length is equal to the product of the average number of collisions C_E and the average path length between any two collisions d_E, which is dependent on the shape of the cavity. Now we consider a spherical integrating cavity of radius r with a diffuse wall and calculate the average photon path length between collisions. Consider a population of photons emitted into the cavity from a small element of the wall surface. Since all parts of the uniform spherical surface are equivalent, the result will apply equally to photons all around the surface. For each photon, let θ be the angle between the photon trajectory and the normal of that element of the surface. The path length of this trajectory from the starting point to the next point of collision is

$$l(\theta) = 2r\cos\theta\ . \tag{2.20}$$

For a Lambertian surface, the radiant intensity from the element of the surface at angle θ is

$$I(\theta) = I_0 \cos\theta\ , \tag{2.21}$$

where I_0 is the radiant intensity at $\theta = 0$. The radiant flux $\Phi(\theta)$ that is emitted from the element of surface in an angular interval $\Delta\theta$ centered on θ, within a solid angle $2\pi\sin\theta\Delta\theta$ is

$$\Phi(\theta) = I(\theta) 2\pi \sin\theta\Delta\theta = I_0 2\pi \sin\theta \cos\theta\Delta\theta\ . \tag{2.22}$$

The total radiant flux emitted from the element of surface is obtained by integrating equation 2.22 over θ:

$$\Phi_{tot} = 2\pi I_0 \int_0^{\pi/2} \sin\theta \cos\theta d\theta = \pi I_0 \,. \tag{2.23}$$

The proportion of the total radiant flux that is emitted in the angular interval $\Delta\theta$ centered on θ is

$$P(\theta) = \frac{\Phi(\theta)}{\Phi_{tot}} = 2\sin\theta\cos\theta\Delta\theta \,. \tag{2.24}$$

$P(\theta)$ can be interpreted as the proportion of the photon population whose trajectories are in the angular interval $\Delta\theta$ centered on θ. Thus the average path length between successive collisions is

$$\begin{aligned} d_E &= \sum_{0}^{\theta=\pi/2} P(\theta) l(\theta) \\ &= 4r \int_0^{\pi/2} \sin\theta \cos^2\theta d\theta \\ &= \frac{4r}{3}. \end{aligned} \tag{2.25}$$

In an empty spherical cavity, the average total path length per photon is the product of the average number of collisions completed by each photon and the average path length per photon per collision, that is

$$l_E = C_E d_E = \frac{4r}{3(1-\rho)} \,. \tag{2.26}$$

Since the reflectivity of wall is very high ($\rho \approx 1$), the average total path length can be very long, usually many meters. Table 2.1 gives some examples of the average total path lengths for different reflectivities for a spherical cavity of radius 5 cm. Fig 2.2 gives a graphical presentation of the trend of the average total path length falling rapidly with decreasing reflectivity.

Table 2.1. Total path length for different reflectivity.

r (m)	0.05			
ρ	0.998	0.992	0.950	0.900
l_E (m)	33.3	8.33	1.33	0.67

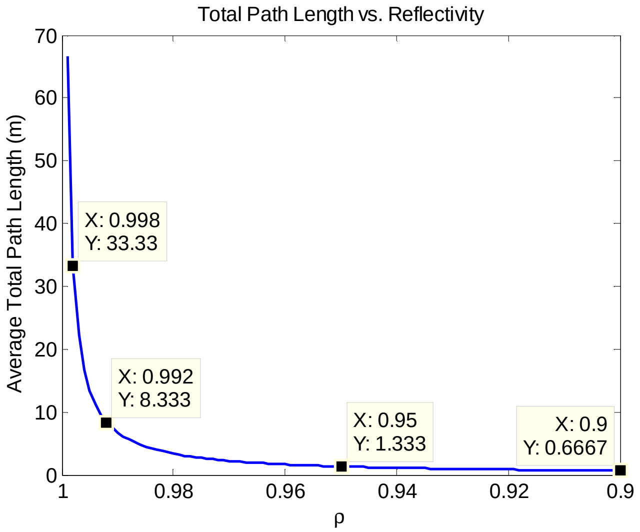

Fig. 2.2. Average total path length vs. reflectivity.

The result above is derived for empty cavity. When the cavity is filled with an absorbing medium, the average total path length will decrease accordingly because some photons are lost in the medium while traveling during collisions. This decrease will be manifested by a decrease in the outward irradiance at the surface of the cavity. The longer the total path length, the greater the probability a photon will be absorbed in the medium and the greater the decrease in the outward irradiance. Hence, a longer path length in the cavity means a greater sensitivity of the apparatus for measurement of small absorption coefficients. There are two ways to obtain long total path length as indicated in the equation. Increasing the physical size of the cavity has practical limits. But, increasing the reflectivity by just a small amount could produce a huge gain in the path length. So, finding the right material with a high diffuse reflectivity in the UV region is critically important.

It is easy to find the average photon path length between collisions for a spherical cavity because of its simplicity and symmetry. For a cavity with other shape, an analytical result may not be obtained easily in the conventional way. In [34], Fry et. al. have shown how difficult it can be just by calculating the average path length for a right cylinder cavity. But fortunately, they have also included a beautiful derivation of the average photon path length between collisions for arbitrary cavity shape, and obtained a general result. The derivation and results are reviewed here.

Consider an arbitrary shape cavity with volume V and total surface area S. Assume the cavity contains n photons per unit volume. Consider an infinitesimal element of surface on the wall dS and an infinitesimal cylindrical element of volume as shown in Fig. 2.3. The number of photons in the cylinder is $n(c\Delta t)(\mu dS)$ where $\mu = \cos\theta$. Since the photon propagation directions have a uniform distribution over the 4π solid angle at any point in the volume, the fraction of the photons propagating in the direction θ, φ in the solid angle $d\Omega = d\mu d\varphi$ is

$$p_\mu = \frac{1}{4\pi} d\mu d\varphi \ . \tag{2.27}$$

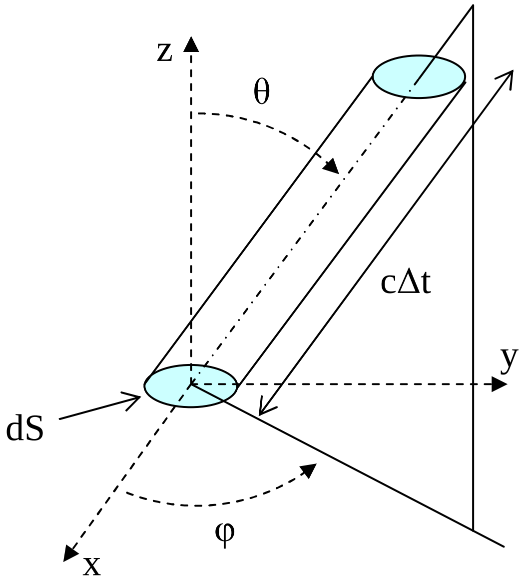

Fig. 2.3. Schematic for photon flux incident on the wall of a cavity.

Therefore the number of photons in the cylinder in Fig. 2.3 that travel in the direction θ, φ in the solid angle $d\Omega$ is

$$dN_\mu = n(c\Delta t)(\mu dS)(\frac{1}{4\pi} d\mu d\varphi) = (\frac{nc}{4\pi})(\mu d\mu d\varphi) dSdt \ . \tag{2.28}$$

All these photons must be supplied by the reflection from the surface. The total number of photons in the cavity is nV and all of these photons will be incident on the wall in an average time d_E/c, where d_E is the average path length between collisions with wall, as defined before. So the total number of photons incident on the wall per unit time per unit area is

$$\frac{nV}{(d_E/c)S}=\frac{nc}{d_E}\frac{V}{S} \tag{2.29}$$

Since the surface is Lambertian, the probability that photons will be reflected in the direction θ, φ in the solid angle $d\Omega$ is

$$p_r=\frac{1}{\pi}\mu d\mu d\varphi\,. \tag{2.30}$$

The photons reflected in the direction θ, φ in the solid angle $d\Omega$ from the element of cavity surface area dS in time dt are contained in the cylinder shown in Fig. 2.3. The number of these photons is

$$dN_r=(\frac{nc}{d_E}\frac{V}{S})(\frac{1}{\pi}\mu d\mu d\varphi)dSdt=(\frac{nc}{\pi d_E}\frac{V}{S})(\mu d\mu d\varphi)dSdt\,. \tag{2.31}$$

To maintain constant radiance, we must have $dN_\mu=dN_r$. It is possible to satisfy this condition because the θ, φ dependences in dN_μ and dN_r are identical in equations 2.28 and 2.31, and we get

$$d_E=4\frac{V}{S} \tag{2.32}$$

This is a general result for a cavity with arbitrary shape. We can use the result that we have obtained for the special case of a spherical cavity for a quick check. For a spherical cavity, $V=(4/3)\pi r^3$, $S=4\pi r^2$ and $d_E=(4/3)r$, just the same as in equation 2.25. This general result has also been checked with other results calculated in a more basic way for cavities with different shapes, e.g. spherical shell and right circular cylinder cavity.

In a practical experiment, a spherical cavity has some fabricating and assembling difficulties, so we usually use a cavity with a cylinder shape. We can apply the general result on a cylinder cavity to obtain the average path length between collisions. For a right circular cylinder with height H and end faces of diameter D, $V=(\pi D^2/4)H$ and $S=\pi D^2/2+\pi DH$. So

$$d_E = 4\frac{V}{S} = \frac{2DH}{D+2H}\,. \tag{2.33}$$

For the special case $D = H$, equation 2.33 gives $d_E=(2/3)D$. It is interesting to note that this result is identical to the d_E for the inscribed sphere that is tangential to all surfaces of the cylinder.

CHAPTER III

INTEGRATING CAVITY ABSORPTION METER

1. Selection of material

As discussed in the previous chapter, the integrating cavities must be constructed with highly reflective diffuse materials in order to obtain a uniform and isotropic light distribution in the cavities and a long effective path length. In the original ICAM, the material Spectralon was used. As stated by the manufacturer Labsphere, “Labsphere’s Spectralon reflectance material is a thermoplastic resin that can be machined into a wide variety of shapes for the fabrication of optical components. Spectralon gives the highest diffuse reflectance of any known material or coating over the UV-VIS-NIR region of the spectrum. The reflectance is generally >99% over a range from 400nm to 1500nm and >95% from 250nm to 2500nm.” [35, 36]. The reflectance of the Spectralon optical grade SRM-99O is plotted against wavelength in Fig. 3.1 and tabulated in Table 3.1.

Table 3.1. Reflectance of Spectralon SRM-99O

Wavelength (nm)	Reflectance
250	0.950
300	0.985
400	0.990
500	0.991
600	0.992
700	0.992
800	0.991
900	0.991
1000	0.993
1100	0.993
1200	0.992
1300	0.992
1400	0.991
1500	0.991
1600	0.991
1700	0.988
1800	0.989
1900	0.981
2000	0.976
2100	0.953
2200	0.973
2300	0.972
2400	0.955
2500	0.950

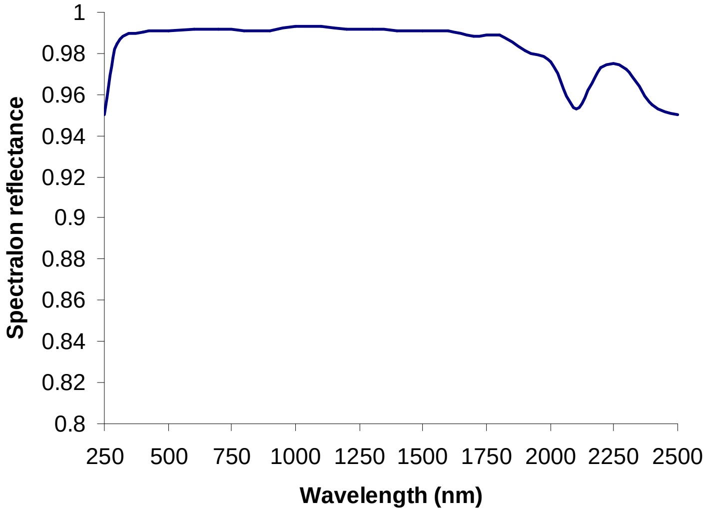

Fig. 3.1. Reflectance of Spectralon SRM-99O.

The reflectance of Spectralon also depends on the thickness of the material. It decreases with decreasing thickness over most of the spectrum. Table 3.2 shows this dependence for several wavelengths, and Fig. 3.2 shows this dependence graphically for wavelength 325nm.

Table 3.2. Reflectance of Spectralon dependence on thickness.

Wavelength (nm)	Thickness (mm)						
	1	2	3	4	5	6	7
325	0.934	0.959	0.970	0.973	0.988	0.985	0.985
450	0.937	0.962	0.973	0.977	0.992	0.991	0.991
555	0.933	0.960	0.972	0.976	0.989	0.989	0.990
720	0.928	0.958	0.970	0.976	0.988	0.987	0.989
850	0.922	0.956	0.969	0.976	0.985	0.986	0.987
1060	0.916	0.954	0.968	0.974	0.986	0.986	0.988

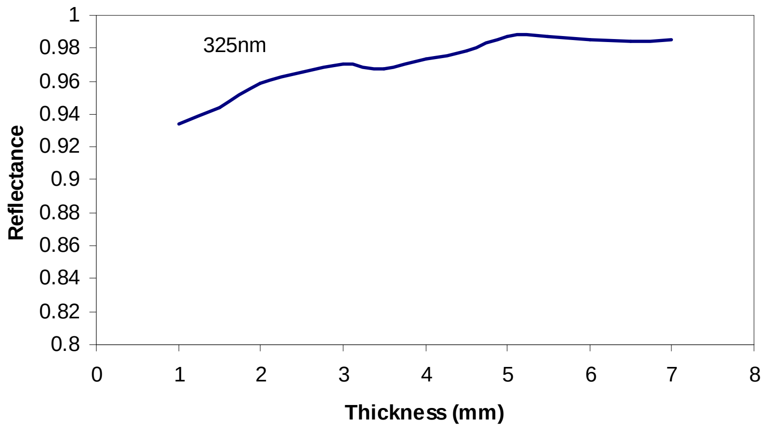

Fig. 3.2. Reflectance dependence on thickness for wavelength 325nm.

In addition to the high reflectance, the surface and immediate subsurface structure of Spectralon exhibits highly Lambertian behavior. This property is quantified by the bidirectional reflectance distribution function (BRDF) [36]. BRDF is defined as the ratio of the radiance of a sample to the irradiance upon that sample, for a given direction of incidence and direction of scatter. The incident direction is specified by two angles: the angle of incidence (θ_i), and the incident azimuth angle (φ_i). Similarly, the scatter direction is specified by the scatter angle (θ_s) and the scatter azimuth angle (φ_s). These angles are defined as in Fig. 3.3. The origin of the coordinate is the point where the central ray of the incident radiation (I) strikes the sample. The z axis is normal to the sample surface, and the x axis lies in the plane defined by the z axis and the direction of I. The incident direction is determined by (θ_i, φ_i), where $\varphi_i = \pi$ by the choice of axis. The scatter direction is determined by (θ_s, φ_s). The solid angle subtended by the detector is Ω.

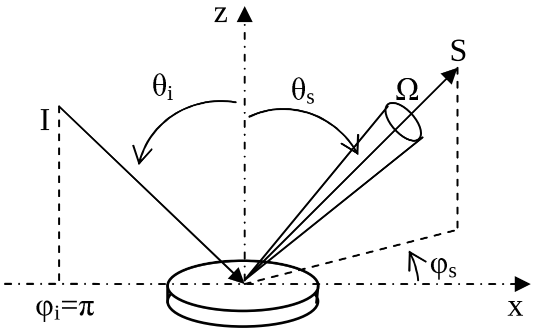

Fig. 3.3. Geometry for the BRDF.

To measure BRDF, the sample is illuminated with a collimated beam from a range of incident directions. A detector, subtending solid angle *Ω*, views the entire illuminated area and can be positioned at a range of scattering directions. The sample irradiance can be calculated from the power P_i incident on the sample and the illuminated area A. The sample radiance L can be calculated from the power P_s collected by the detector, the detector solid angle, and the area of illumination. The sample BRDF is then calculated as the ratio of these two quantities:

$$BRDF \equiv \frac{radiance}{Irradiance} = \frac{P_s/(\Omega A\cos\theta_s)}{P_i/A} = \frac{P_s}{P_i\Omega\cos\theta_s} \tag{3.1}$$

The BRDF of a perfectly diffuse, i.e. Lambertian, sample should be constant for all bidirectional geometries. It should be noted, however, that the power P_s collected by the detector is dependent on the scatter angle θ_s, and becomes very small as θ_s approaches π/2. So the effects of system noise, and other sources of measurement error, become much more serious at large scatter angles.

BRDF measurements are also dependent on any polarization bias of the detector and source of illumination. Fig. 3.4 presents the BRDF for Spectralon, under linearly polarized illumination, where the direction of polarization is parallel (*P*) to the plane of incidence [36]. The detector is also polarized, with bias parallel (*P*) or perpendicular (*S*) to the plane of incidence. For a material which does not affect the polarization of the incident flux, the observed BRDF for the cross-polarized configuration (*PS*) would be zero. For a perfect depolarizing sample, BRDF values would be identical for the two measurement configurations. The measurements in Fig. 3.4 were made in plane, that is, the detector was placed in the plane defined by the incident beam and the normal to the surface of the sample. The dependence on φ_s was ignored. The flatness of the BRDF shows that Spectralon is indeed a fairly good diffuse reflector.

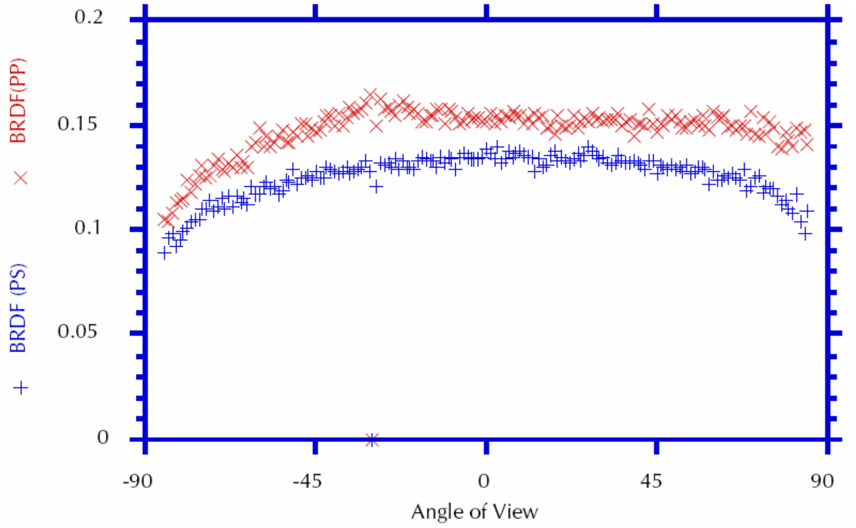

Fig. 3.4. BRDF of Spectralon. (Incident angle 30°)

Spectralon's high reflectance in the visible ensures a long total effective path length and thus high sensitivity of the ICAM. But a steep drop in reflectance below around 350 nm makes the material not suitable for the UV region. Note that for a spherical cavity with diameter of 10 cm and wall reflectance of 95% for wavelength of 250 nm, the effective path length is just 1.3 m, much less than the 8.3 m for wavelength of 400 nm. Even worse, the exposure of Spectralon to UV illumination would decrease the reflectance. As stated in the manufacturer's document [36], "Spectralon test samples were exposed to deep and mid-UV (unfiltered Hg arc lamp) at a vacuum of $\leq 10^{-6}$ torr with the equivalent of 2 suns for 500 equivalent sun hours. At 110 sun hours, a lowering of reflectance of between 5 - 10 % in the UV was noted; at 500 sun hours, a slight yellowing in the VIS was noted, along with a 20% total drop in the UV (250 nm)." The reflectance could drop to 75% for 250 nm after extended exposure to UV illumination, which corresponds to a total effective path length of only 0.15 m! This "aging" effect of Spectralon under exposure of UV light has also been investigated [37, 38]. In our measurement of the pure water absorption coefficient in the UV, the ICAM cavities have been under UV illumination for years and the drop of reflectance could be significant. This reflectance change also makes frequent calibration necessary; this is time consuming and can make the measurement results less reliable. Previous studies in our group have shown that the ICAM made of Spectralon gave poor results [39]. Random noise is overwhelming due to the drop of total effective path length at wavelengths below 350 nm. The absorption of Spectralon in the UV also gives an apparent increase in water absorption because some light actually penetrates into the Spectralon wall. As we fill up the sample cell with water, more light is penetrating into the wall and absorbed by Spectralon, which appears as the absorption of water. Thus in order to measure the pure water absorption coefficient in the UV region, a search for new material that is suitable for building the ICAM was required.

It is necessary to understand the nature of diffuse reflective materials before undertaking a search. Consider a light beam striking the surface of the sample. The interaction between photons and the sample occurs not only at the surface, but also within the material for a small depth. Photons end up in three ways. First, some photons enter the material, are scattered by the particles many times and eventually come out of the material on the same side as they go in. These photons are reflected. If the scattering is totally random, then this reflection is diffuse. Second, some photons are absorbed by the particles and lost permanently. Third, some photons, after many scattering, will find their way through the material and come out from the other side. These photons are transmitted. For a highly reflective material, absorption and transmission must be minimized.

Fused silica is a material widely used in optics and well known for its low absorption over a broad bandwidth. It is essential just silicon dioxide (silica or SiO_2). Its optical absorption is virtually zero in the visible and can also be made low in the UV if impurities are removed. Fig. 3.5 shows the transmittance of Corning's HPFS Standard Grade fused silica, which is a high purity synthetic amorphous silicon dioxide manufactured by flame hydrolysis. The internal transmittance of HPFS at wavelength of 185 nm is certified to meet the condition $T_{internal} \geq 88\%/cm$.

Fused silica is used in many areas of the industry and academic research. It can be purchased at a reasonable price. Many companies sell and custom fabricate fused silica apparatus. So fused silica is an excellent candidate material for our application because of its high quality and wide availability.

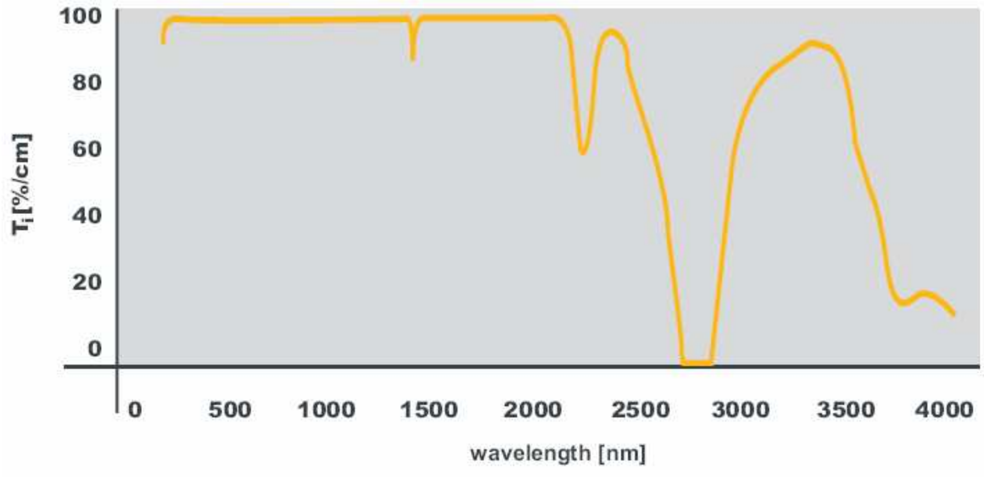

Fig. 3.5. Internal transmittance of Corning HPFS standard grade fused silica.

Conventional quartz products are in the form of plates. A piece of quartz plate has high transmittance, seemingly having nothing to do with high reflectance. But a simple model can show that, if properly arranged, a number of highly transparent quartz plates together can exhibit a very high reflectance [40]. See Fig. 3.6.

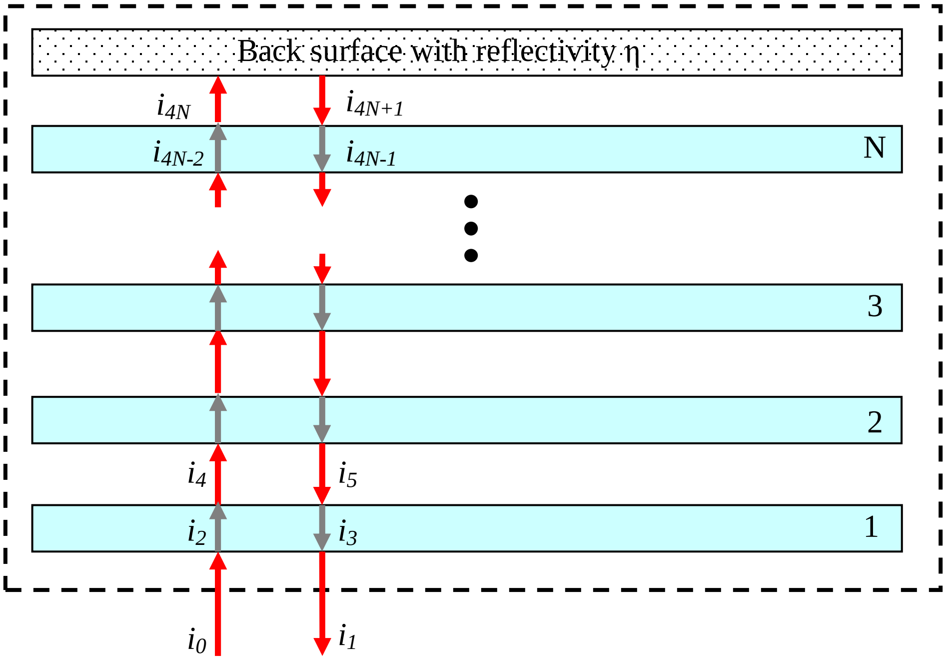

Fig. 3.6. A reflector made of N pieces of quartz plates and back reflecting surface.

Consider N quartz plates placed parallel to each other to form a pile. The distance between any two plates is not essential. Light incident normally on the surfaces of the plates undergoes a series of reflections at the quartz air interfaces. The net reflectance is given as $R_N = i_1/i_0$. Let ρ be the reflectance at each quartz air interface, η be the reflectance at the back surface. Let i_n be the light intensity traveling down the direction as shown in Fig. 3.6. For the case of only one quartz plate, we can write the following equations for i_n:

$$i_1 = i_0\rho + i_3(1-\rho) \tag{3.2}$$

$$i_2 = i_0(1-\rho) + i_3\rho \tag{3.3}$$

$$i_3 = i_2\rho + i_5(1-\rho) \tag{3.4}$$

$$i_4 = i_2(1-\rho) + i_5\rho \tag{3.5}$$

$$i_5 = i_4\eta \quad . \tag{3.6}$$

Solving these simultaneous equations gives the net reflectance R_1,

$$R_1 = \frac{i_1}{i_0} = \frac{\eta + 2\rho - 3\eta\rho}{1 + \rho - 2\eta\rho} \, . \tag{3.7}$$

For the case of two quartz plates, the relationship between i_5 and i_4 is just the relationship between i_1 and i_0 in the one quartz plate case. So we replace equation 3.6 with the following equation

$$i_5 = i_4 R_1 \, . \tag{3.8}$$

Clearly now R_1 is in the place of η. So to get R_2, we simply use equation 3.7 but replace η with R_1. After some algebra, we get

$$R_2 = \frac{\eta + 4\rho - 5\eta\rho}{1 + 3\rho - 4\eta\rho} \, . \tag{3.9}$$

Doing this again, i.e. replacing η with R_2 in the above equation, we get the reflectance for a three quartz plate pile

$$R_3 = \frac{\eta + 6\rho - 7\eta\rho}{1 + 5\rho - 6\eta\rho} \, . \tag{3.10}$$

After using some reasoning and calculating, we get the final result for the reflectance of an N quartz plate pile

$$R_N = \frac{\eta + 2N\rho - (2N+1)\eta\rho}{1 + (2N-1)\rho - 2N\eta\rho} \, . \tag{3.11}$$

It is easy to check that for large *N*, no matter what values ρ and η take, the reflectance approaches unity. For a quartz air interface, ρ is 0.04. Fig. 3.7 shows the reflectance dependence on the number of layers of quartz plates for different η values.

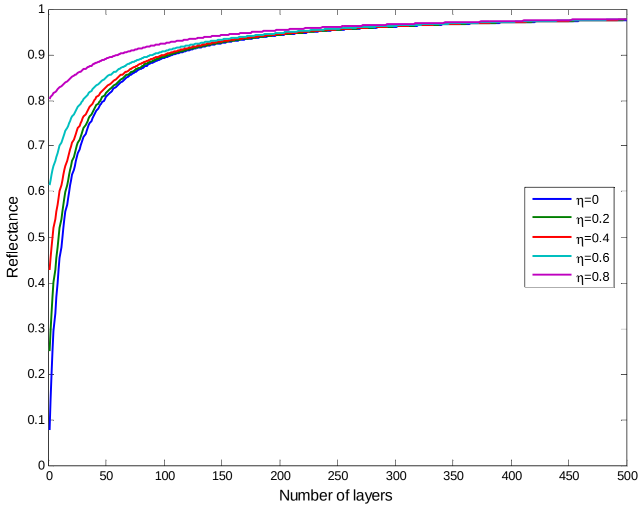

Fig. 3.7. Reflectance of a pile of quartz plates for different η values. $\rho=0.04$.

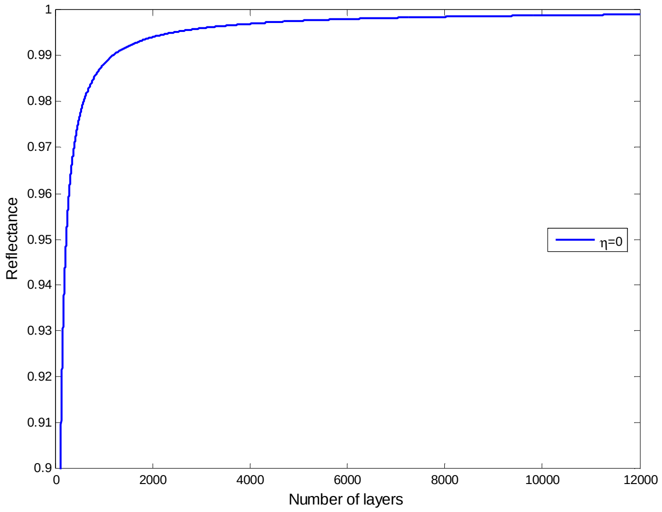

Fig. 3.8. Reflectance dependence on the number of layers. $\rho=0.04, \eta=0$.

We can see that for sufficiently large N, the reflectance does not depend on the value of η, as we expected. Fig. 3.8 shows the dependence of the reflectance on the number of layers for $\eta = 0$ and $\rho = 0.04$. The reflectance reaches 0.999 at $N \approx 11500$. For a normal quartz plate with thickness of about 2 mm, it means that a total thickness of 23 m is needed. The essence of this simple simulation is that multiple small reflections can build up to reach very high reflectance. Although using many quartz plates is not practical, we can use submicron sized quartz particles packed together to achieve the same goal: multiple reflections. We use 1 cm for a reasonable estimation of the thickness of the apparatus we are going to build. To achieve a reflectance of 0.999, the size of each particle should be on the order of 1 μm. We should be reminded that in the derivation above, we have neglected the absorption of the material. For light passing through 11500 layers of quartz plate (or particles), even a small absorption can cause significant degradation in reflectance. We have known that, in quartz, impurities are the main causes of absorption. So we need a material composed of high purity quartz particles with sizes around one micron or less.

2. Fumed Silica

At first our group tried to make our own quartz powder and observed the high reflectivity and diffuse nature of the powder [40]. But soon, it was realized that commercial high purity quartz powder exists with the name of fumed silica. Aerosil is a line of fumed silica products from Degussa. It is silicon dioxide powder made from vaporized silicon chloride, oxidized in high temperature flame with H_2 and O_2. In this reaction, hydrogen chloride (HCl) is the only byproduct which can be easily separated as it remains in the gas phase. Content of trace elements can be made very low. The SiO_2 content, by weight, can be as high as ≥ 99.98%. The average primary particle size can be a few nanometers to several tens of nanometers. The base particles are not found alone. They form aggregates, which then form agglomerates. Fig. 3.9 and Fig. 3.10 show SEM pictures of fumed silica aggregates and agglomerates [41].

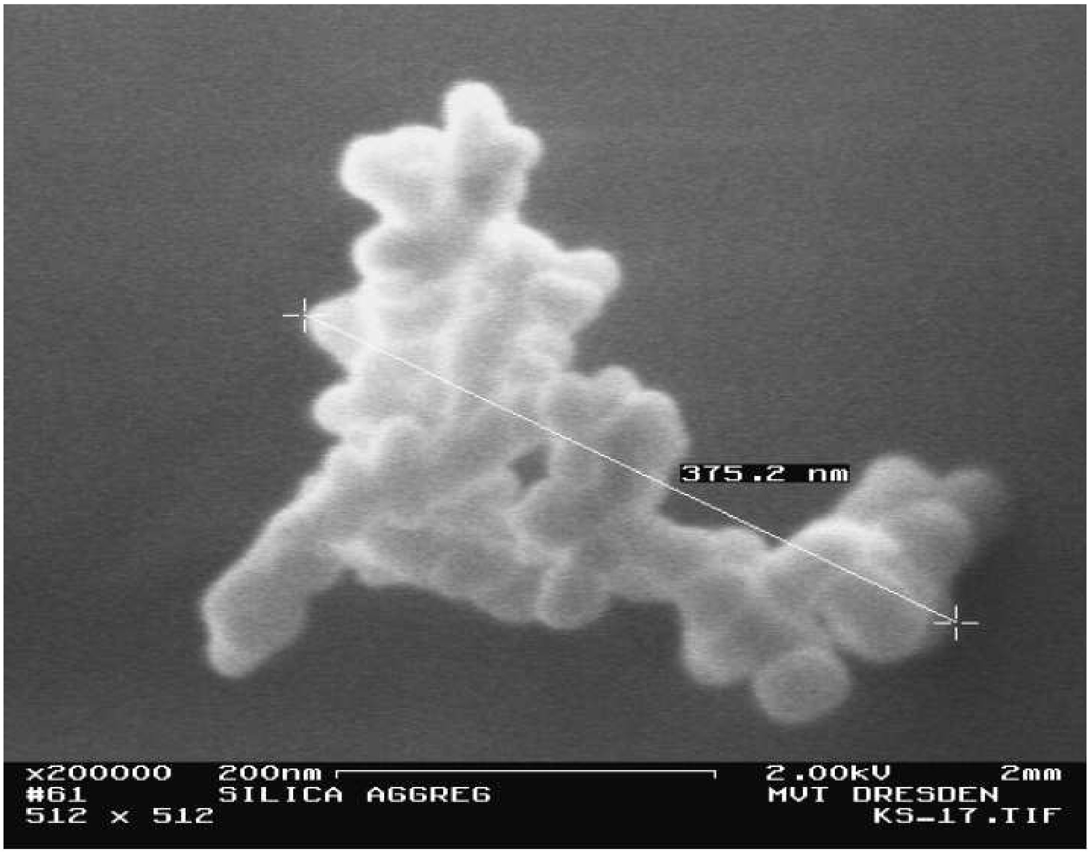

Fig. 3.9. Fumed silica aggregate.

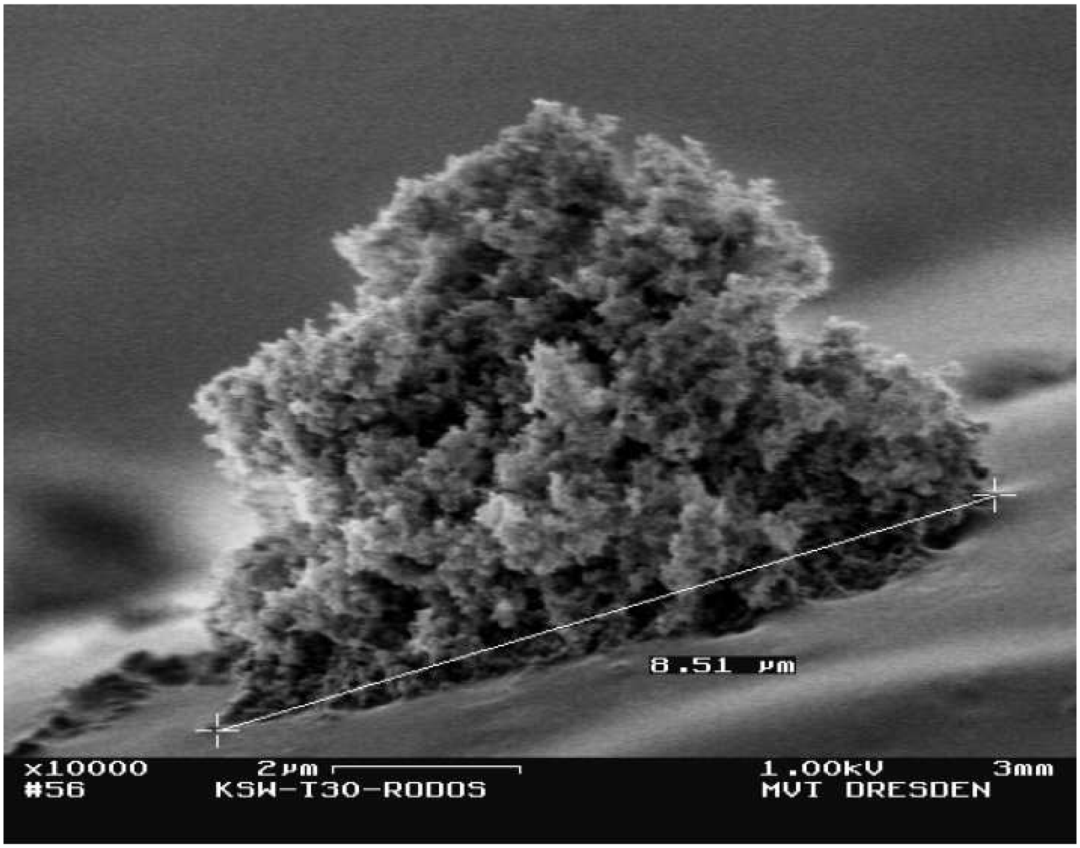

Fig. 3.10. Fumed silica agglomerate.

Several Aerosil products, i.e. Aerosil 380, Aerosil 90 and Aerosil EG 50, were tested for their reflectivity and diffuse property [40]. To compare the reflectivity of the quartz powder (in this dissertation, quartz powder, although not exact, means the same thing as fumed silica does.) and that of Spectralon, a setup as shown in Fig. 3.11 was used. Samples were rotated under an integrating cavity so different samples were exposed to the laser beam alternatively through a small port on the cavity. The laser beam was incident on the samples at an angle of 8° from normal. The reflected light was collected by the integrating cavity and measured by a Hamamatsu 1P21 photomultiplier tube

(PMT), which was mounted on the side of the cavity. A baffle was used to prevent any light from reaching the PMT directly from scattering off the surface of the samples. The result is shown in Fig. 3.12.

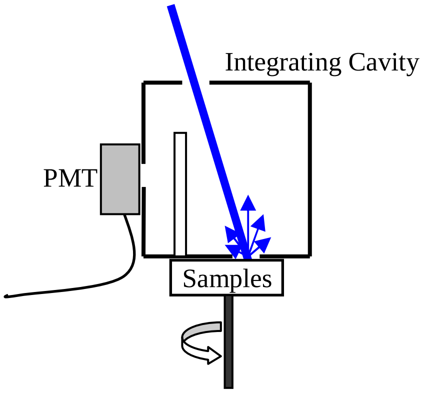

Fig. 3.11. Setup to compare the reflectivity of Spectralon and several fumed silica samples.

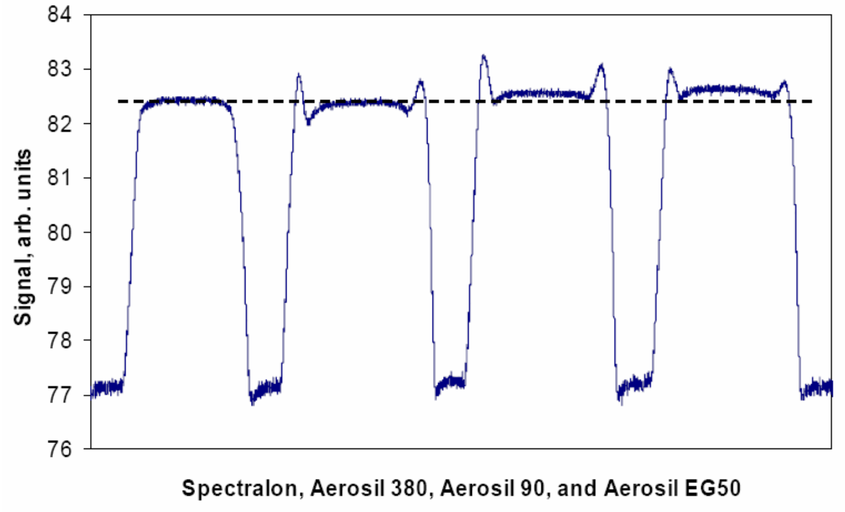

Fig. 3.12. Relative reflectivity of Spectralon and several fumed silica samples.

From Fig. 3.12, it is clear that Aerosil 90 and Aerosil EG 50 both have higher reflectivity than Spectralon, while Aerosil 380 has almost the same reflectivity as Spectralon. The "dog ears" in the graph are due to the specular reflections from the metal rings that were used to support the samples.

In the above experiment, it was shown that the Aerosil samples outperform Spectralon in reflectivity when compared relatively. More knowledge could be gained if we know the absolute reflectivity of the Aerosil samples. There is a way to do this. Consider the cavity as shown in Fig. 3.13. The wall of this cavity is made of the highly diffuse reflective material that is under investigation. The cavity is closed except for one small opening for an optical fiber carrying light in or out the cavity. Suppose that at one infinitesimal time interval, a population of photons is released into the cavity through the fiber. Then the outward irradiance is sampled using the same fiber. An exponential decay in the irradiance is expected. The time constant of this decay τ is determined by the absolute reflectivity of the wall as given below

$$\tau = -\frac{1}{\ln \rho} \frac{\bar{d}}{c}, \tag{3.12}$$

where ρ is the reflectivity of the wall, $\bar{d}$ is the average distant between collisions as discussed in the previous chapter, and c is the speed of light.

Plotting out the time response of the irradiance and fitting it with an exponential function, we can calculate the reflectivity of the material ρ using τ and $\bar{d}$.

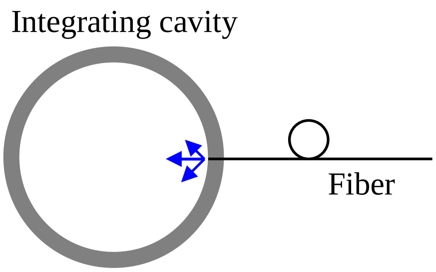

Fig. 3.13. Setup to measure the absolute reflectivity of material.

In the real measurement, a cylindrical cavity with both the diameter and the height equal to 5 cm was used [40]. The thickness of the wall was also 5 cm. Two fibers were used to minimize the interference between the input and output pulses. Light was introduced into the cavity by a multimode fiber. Another identical fiber located 90 degree apart from the input fiber was used to sample the outward irradiance. A Hamamatsu 1P21 photomultiplier tube was used for the detector. Fig. 3.14 shows the typical shapes of the input pulse, the output pulse and the exponential fit to the output pulse. From the exponential fitting parameters, the reflectivity was determined as 0.998 at wavelength of 532 nm, and 0.996 at wavelength of 266 nm. Both were believed to be the best diffuse reflectivity ever measured at the respective wavelength. For Spectralon, the reflectivity is ~ 0.991 at 532 nm and ~ 0.96 at 266 nm. The advantage of the fumed silica as a UV diffuse reflector is obvious.

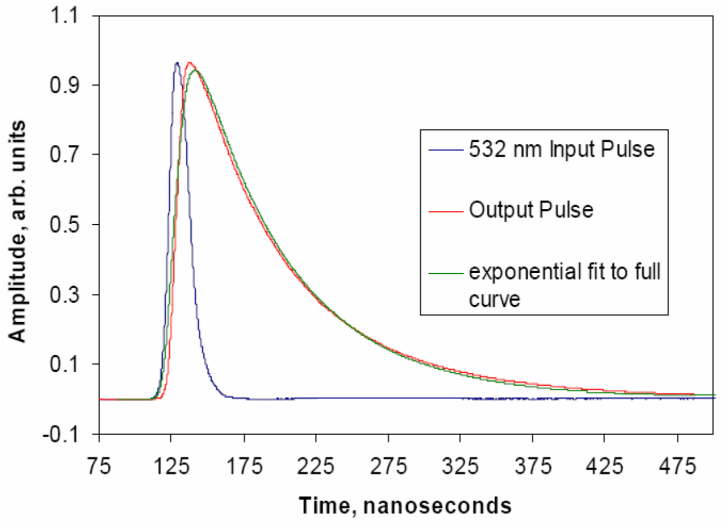

Fig. 3.14. Typical shapes of the input pulse, the output pulse and the exponential fit to the output pulse in the absolute reflectivity measurement.

The bidirectional reflectance distribution function (BRDF) was also measured [40]. The setup is shown in Fig. 3.15. A collimated laser beam hit the surface of a reflective diffuse sample from a specified angle. The detector was swung above the sample from a fixed distance across the angle from -90° to 90°.

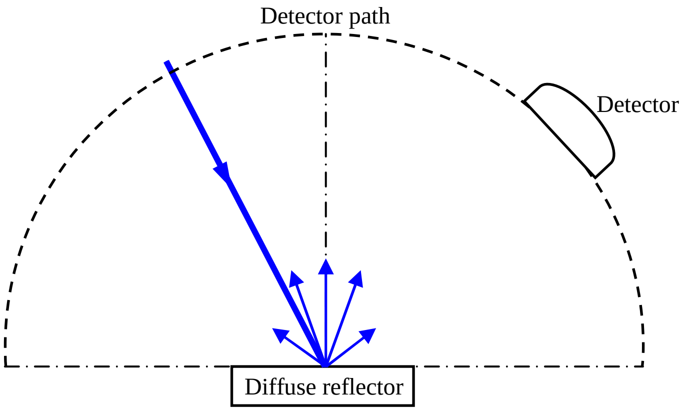

Fig. 3.15. Setup to measure the BRDF of a diffuse reflector sample.

The BRDFs of Spectralon and Aerosil samples were measured and compared in Fig. 3.16 for several different wavelengths. The curves have been offset to facilitate visual presentation. It is clear, from the experimental results, that the Aerosil sample is performing better than or equivalent to the Spectralon sample, if we remember that a more constant BRDF means a better diffuse reflector.

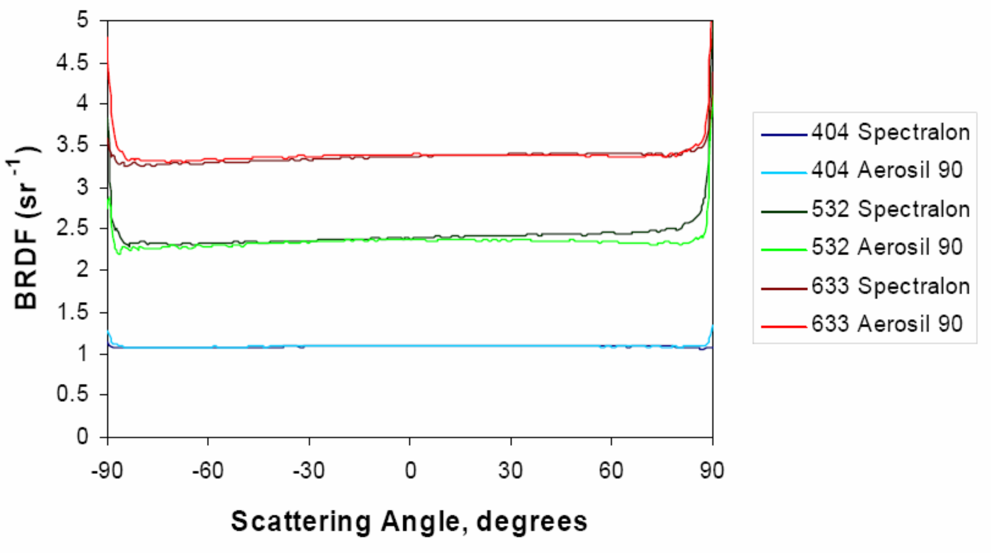

Fig. 3.16. Comparison between BRDFs of Spectralon and Aerosil samples at three different wavelengths.

In the measurements of the reflectivity and BRDF, fumed silica outperformed Spectralon in every aspect, with a more noticeable advantage in UV. We have already known that Spectralon was considered to "give the highest diffuse reflectance of any known material or coating over the UV-VIS-NIR region of the spectrum." So we have developed an excellent material that potentially could replace Spectralon in many important applications where high reflectivity is critical, especially in the UV. It should also be noticed that fumed silica doesn't have the problem of deterioration under exposure to UV illumination. The fumed silica has two disadvantages. First, due to the fine powder nature of the fumed silica, it is fluffy and occupies a large volume, most of which is empty space. Consequently, it must be pressed into a relatively small volume in order to achieve the desired reflectivity. Although at this point it is a semi-solid, it still should be supported in a container to maintain a specific shape (More recently, stable forms have been obtained after firing in a kiln). In this work, to make a cylindrical cavity, two cylindrical tubes with the right size were cut and properly assembled. Then the fumed silica was packed between the two tubes, just like a sandwich. The fumed silica was pressed while packing. The transmission of fumed silica samples under different pressures was investigated [40]. Second, due to the large surface area of the material, moisture and other volatile materials are readily absorbed. The resulting contamination lowers the reflectivity. Consequently, the powder is baked at a high temperature to eliminate moisture and other volatile contaminants. All our fumed silica is baked before being used to build our research apparatus.

3. Integrating cavity assembly

Fig. 3.17a and 3.17b show cross sections of the integrating cavity assembly parallel and transverse to the Z axis.

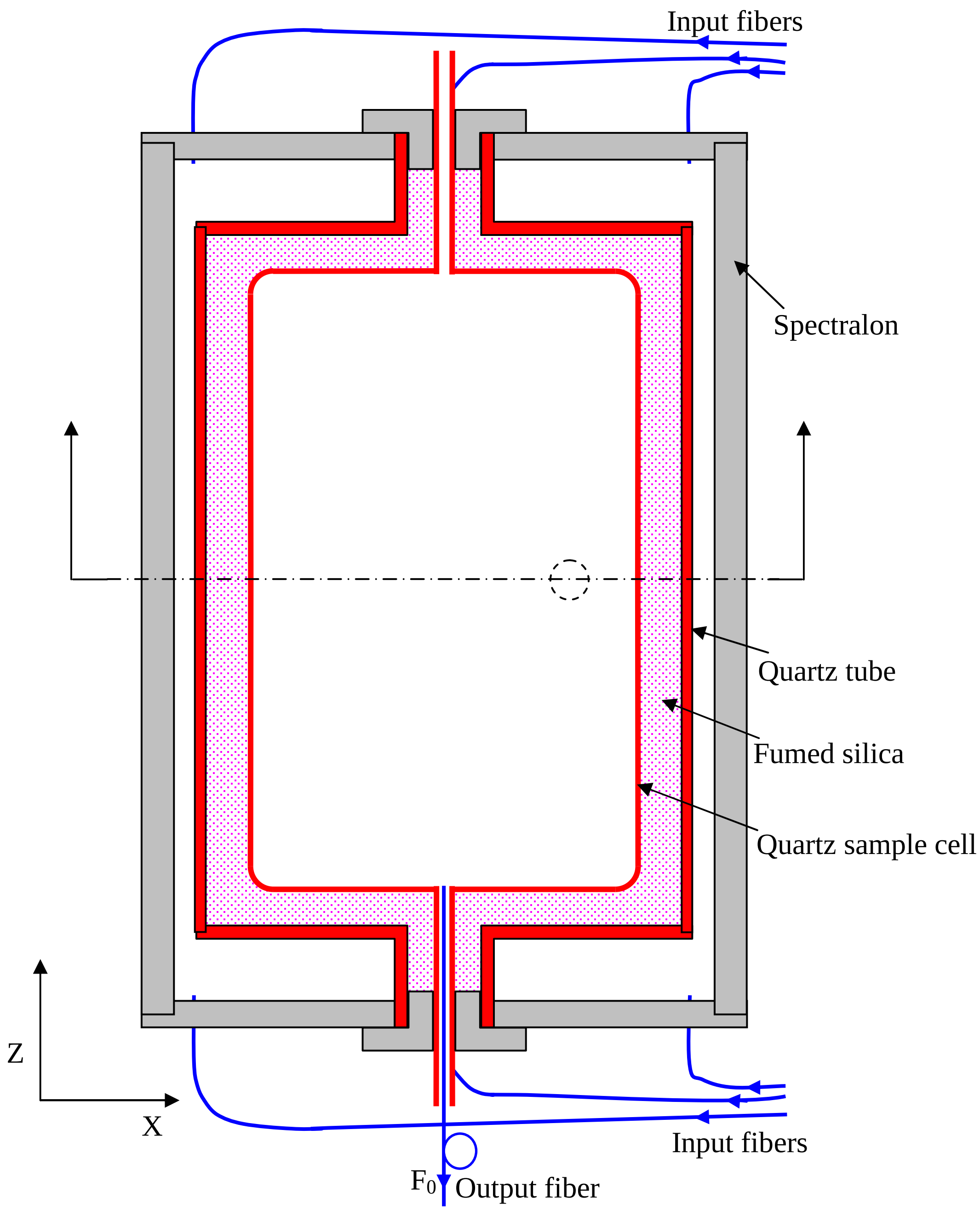

Fig. 3.17a. Cross sections of the integrating cavity. Side view.

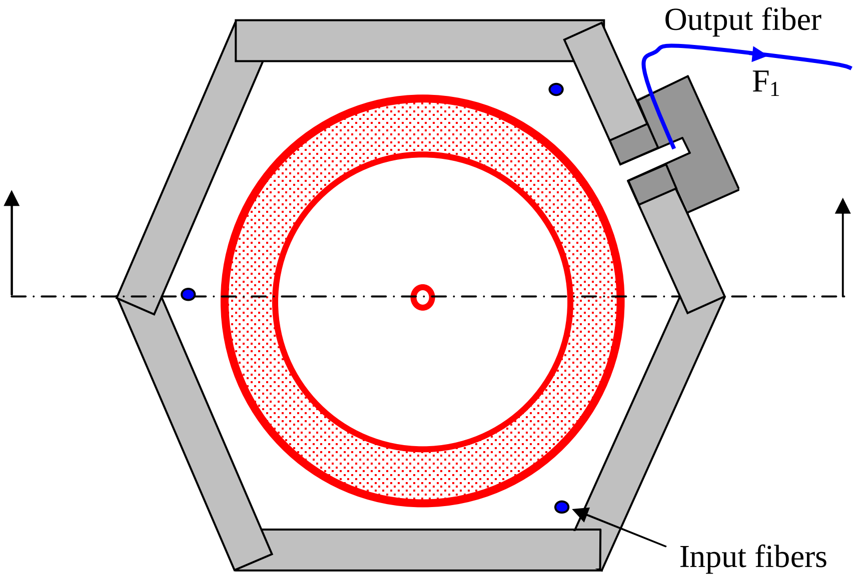

Fig. 3.17b. Top view.

The assembly consists of two concentric integrating cavities. The outer cavity has a hexagonal cross section with 107 mm across the inside faces. Its wall is made of six interlocking Spectralon plates attached to each other by nylon screws. Each plate is 12.7 mm thick and 254 mm high. Two 19 mm holes were drilled on two plates in order to mount the sampling fibers in previous experiments. In the present experiment, only one hole located at the center of one plate was used to sample the irradiance in the outer cavity and the other hole was plugged. A Spectralon cup with 19 mm OD and 4.8 mm ID is inserted into the hole and terminated at the inner surface of the plate. An optical fiber was inserted through the side of this cup, to sample the irradiance in the outer cavity. The fiber is Thorlabs catalogue number FT-800-UMT. The diameter of the core is 800 μm, and the numerical aperture (NA) is 0.37. The fiber carries the light to a chopper box, where it is modulated and then detected by a photomultiplier tube. The ends of the outer cavity are closed by two hexagonal Spectralon caps 12.7 mm thick. Each hexagonal cap has a 19 mm center hole for the quartz sample cell inlet and outlet tubes. End cap also has three 2 mm holes to insert the six input fibers that deliver light to the outer cavity. The three holes are on a 113 mm diameter circle, 120° apart. On each cap they are offset by 60° with respect to those on the opposite cap. The input fibers have a 600 μm core diameter and a 1.0 mm nominal overall diameter. The ends of the input fibers are arranged in a vertical linear array that collects light over the height of the exit slit of a monochromator. The other ends are inserted into the holes on the Spectralon end caps. The arbitrary choice of six input fibers provides direct illumination of the entire outer cavity. However, the diffuse reflectivity of the Spectralon is so high that even one fiber would have probably been sufficient to provide the required uniform illumination of the sample volume.

The inner cavity is enclosed by the fumed silica packed between two fused silica cells. The sample cell is made of Suprasil tube from Heraeus Quartz with 88 mm OD. The main body is about 135 mm long and tapers into a 125 mm long, 5 mm ID, 7 mm OD quartz tube at each end. The tubes are used to fill and empty the cell. The taper is necessary to avoid trapping air at the top of the cell when filling and to avoid leaving water at the bottom when draining. The capacity of the sample cell is 566 ml. The outside surface of the main body is heavily frosted in order to minimize specular reflection effects when light enters the cell through the quartz air interface. The out side of the fumed silica region is a tube made of the TOSOH ED-H synthesized fused silica with 96.5 mm ID and 105 mm OD. The tube is 152 mm long. Two end caps are made of the TOSOH ES fused silica ground disc with a 105 mm diameter and a 20 mm diameter center hole. To make the structure strong, the bottom cap is welded together with the tube. On each end cap, a Suprasil 300 fused silica tube is welded. The tube has a 17 mm ID and a 20 mm OD. Fumed silica is packed between the two fused silica cells. When packing, a small amount of fumed silica is put in the space between two cells and then a small quartz rod is used to press the fumed silica down until the powder feels solid. Then more fumed silica is used. It is a tedious process to pack the fumed silica; a lot of patience and experience is required. A dark room and a flashlight help to check the uniformity of the fumed silica wall. For example, illuminating the sample cell using the flashlight and observing from the outside, a bright spot indicates a place where fumed silica is packed too loose and needs to be fixed. At the ends of the cavity, the fumed silica is sealed with two Spectralon plugs. An output fiber is placed in the sample cell through the outlet tube at the bottom of the cell to sample the outward irradiance in the inner cavity. The fiber has the same specifications as the one used to sample the irradiance in the outer cavity.

Samples are delivered to the sample cell through quartz tubing connected by Tygon high purity plasticizer free tubing. Use of Tygon tubing is minimized to avoid contact of pure water with any material other than quartz. The entire integrating cavity assembly is placed in a small dark space built up with light shielding cloth, so that stray light is minimized. Any tubing or fiber that enters the cavity is covered with shielding cloth, because environmental light can easily propagate through these glass waveguides into the cavity and contribute a noisy background. Because the light source is weak in the UV, it is especially important to avoid a stray light background. During the experiment, the room lights are turned off to further minimize any background light.

CHAPTER IV

PURE WATER SYSTEM

1. Pure water specification

Absolute pure water is hard, if not impossible, to obtain in the laboratory because, in part, pure water will attack the container and quickly absorb contaminants from the environment. Many early measurements of absorption on pure water are flawed because of the quality of the water used. Some researchers used plastic or Pyrex containers and reported that the absorption increased after extended storage of pure water sample in the containers. Some of the previously accepted water purification methods are not able to produce ultra pure water. For instance, water triply distilled in a quartz vessel still contains some organic materials with low boiling points. Organic or microbial contaminants can be removed by UV treatments, but that reduces the resistivity of the water.

Many professional organizations have published standards to specify the quality of pure water, such as the American Chemical Society (ACS), the American Society for Testing and Materials (ASTM), the College of American Pathologists (CAP), the International Organization for Standardization (ISO) and the National Committee for Clinical Laboratory Standards (NCCLS). In the standards, water is classified according to the electrical resistivity, organic or microbial contaminants and other contaminants present. The electrical resistivity is used to indicate the ion content in water. The organic contaminants can often be specified by the total organic carbon (TOC), which is a critical parameter to our experiment because any organic contaminants will adversely affect our measurement of the optical absorption in UV. The ASTM D-19 Standard for Electronic Grade Water specifies type I water as having a minimum resistivity of 18 megohm-cm and a maximum TOC of 25 μg/liter. Type II electronic grade water is specified as having a minimum resistivity of 17.5 MΩ-cm and maximum TOC of 50 μg/liter. In other standards, the type I and type II may have different specifications. In our project, we have traditionally adopted the definition that the type II water has at least a 1.0 megohm-cm resistivity at 25°C. And our type I water is the final product from our commercial water purification system; it consistently has a resistivity of 18 megohm-cm and a TOC of < 5ppb.

Many types of water purification methods are available, such as distillation, active carbon adsorption, microporous membrane filtration, reverse osmosis (RO), electrodeionisation, UV treatment, and ultrafiltration. Every method has its own advantages and disadvantages. Modern water purification systems use a combination of several methods to obtain ultra pure water.

2. Water purification system

We use a commercial water purification system from Millipore to produce the ultra pure water for our experiments. The system consists of three subsystems: an Elix 10, 60 liter polyethylene storage tank, and a Milli-Q Gradient A10. The Elix 10 is the pretreatment unit, which will produce type II pure water. The Milli-Q subsystem is the polishing unit, which will produce type I pure water. Because Elix 10 is slower in production rate than the Milli-Q system, the 60 liter tank is used to store type II water produced by the Elix 10. The Milli-Q is thereby provided with a sufficient water supply when a large amount of ultra pure water is needed. When the Elix 10 has filled the tank, it is shut off by a water level sensor in the storage tank. The tank is made of polyethylene, which is the best material for storage of pure water according to Millipore. Fig. 4.1 is a block diagram of the water purification system.

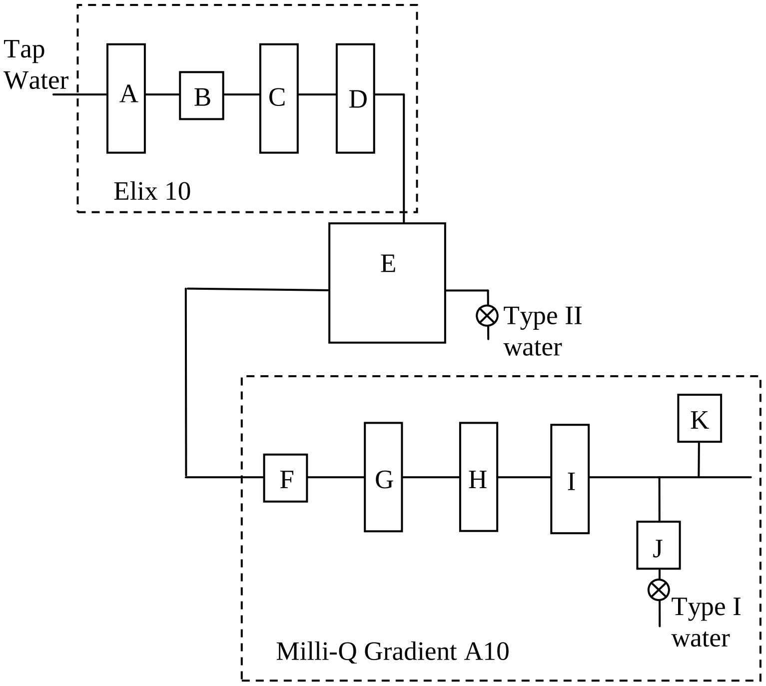

A. Progard pretreatment pack
B. Booster pump
C. Reverse osmosis (RO) cartridge
D. Electrodeionization (EDI) unit
E. 60 L polyethylene tank
F. Pump
G. Q-Gard cartridge
H. UV lamp
I. Quantum ultra-pure cartridge
J. 0.22 μm final filter
K. A10 TOC monitor

Fig. 4.1. Block diagram of the Millipore water purification system.

The Elix 10 produces type II water from the tap water by combining several purification technologies. Tap water passes through a Progard pretreatment pack first, which is designed to remove particles and free chlorine from the feed water. In addition, it helps to prevent mineral scaling in hard water areas. The water is then pressurized by a pump and sent through a reverse osmosis (RO) cartridge to generate intermediate quality water. Next, the RO product water passes through an electrodeionization (EDI) module to reduce levels of organic and mineral contaminants. The typical resistivity of water produced by Elix 10 is 10 - 15 megohm-cm and the total organic carbon (TOC) is less than 30 ppb (μg/liter). The product water is then stored in the 60 L polyethylene tank. The tank has a vent filter on the top cover to prevent bacteria or any air borne contaminant from entering the tank. An overflow tube on the side prevents overfilling. A valve at the bottom provides access to type II water directly from the tank for rinsing pure water containers.

The Milli-Q system is used as a final water purification stage, or so called “polishing” stage. The feed water comes from the 60 L polyethylene tank. It produces ultra pure water, which is equal to or better than ASTM, CAP and NCCLS type I water quality standards. Feed water enters the system and is pumped through the Q-Gard cartridge for an initial purification. Then the water is exposed to UV light at both 185 nm and 254 nm to oxidize organic compounds and kill bacteria. The function of the Quantum cartridge is to remove trace ions and oxidation by-products produced by the action of the UV light. The ultra pure water is obtained after this cartridge. A manual 3-way valve directs ultra pure water through a final 0.22 μm membrane filter so that any particles or bacteria greater than 0.22 μm will be removed. An A10 TOC monitor is installed to sample the ultra pure water and determine trace organic levels. This special feature makes real-time organic content monitoring a reality. The final product of the water system consistently has an electrical resistivity of 18.2 megohm-cm and TOC of 3 – 4 ppb. It is maintained at a stable temperature of 25 ± 1 °C.

3. Sample preparation

The water purification system is installed in the same room as the ICAM, so fresh type I pure water can be used whenever ultra pure water is needed. Most containers are made of Pyrex glass; some critical ones are made of quartz. Storage vessels made of plastic are avoided because ultra pure water can slowly leach organic contaminants from the container wall and adversely affect our measurements in the UV. Plastic tubing used for transporting the pure water sample is not avoidable, but is limited to the minimum possible. Whenever flexible tubing is needed, Tygon high purity plasticizer free tubing is used. Tygon tubing is chosen for its high purity and flexibility. Quartz tubing is used wherever rigid tubing is acceptable.

All glassware, including Pyrex or quartz containers, measuring cylinders and pipettes, were initially soaked in an acid cleaning solution, which was made by dissolving potassium dichromate in type II water and then mixing with concentrated sulfuric acid. This solution, also known as “chromic acid”, is widely used in the chemistry laboratories for cleaning glassware. The glassware was then rinsed with type II pure water at least 5 times and subsequently rinsed with type I ultra pure water at least 3 times. It was then filled or immersed with type I water for at least one week before use.

CHAPTER V

APPARATUS

1. System overview

The ICAM system was developed originally by Pope and then modified by Cui and Lu [39, 42, 43]. The current system was improved to facilitate measuring small absorptions in the UV. The system includes both hardware and software components. The hardware components produce signals, S_0 and S_1. The software components automate data acquisition, control hardware components, and provide signal processing and analysis. Fig. 5.1 is a block diagram of the ICAM system.

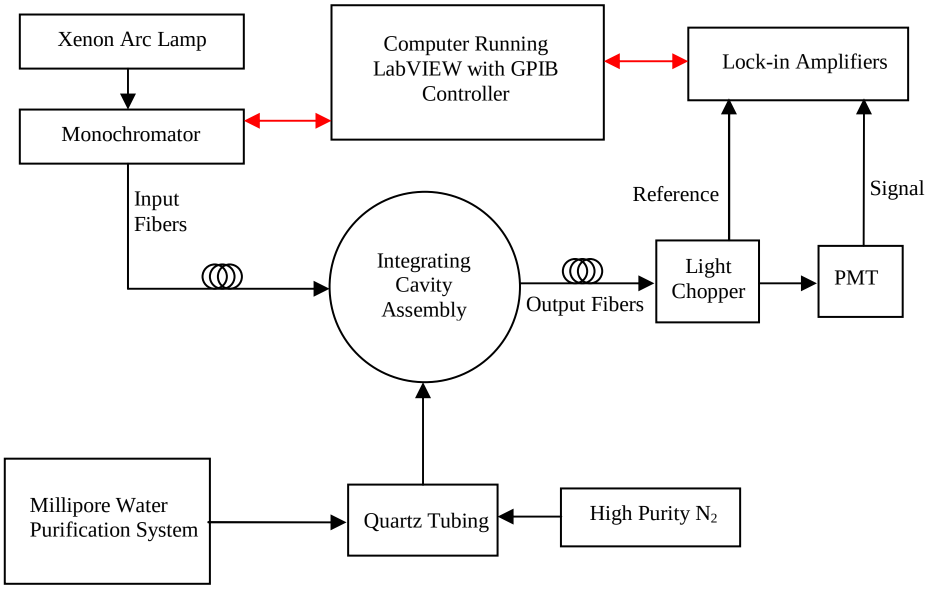

Fig. 5.1. Block diagram of the ICAM system.

2. Illuminating components

For illumination purposes, a broad band light source is used. Light produced by the source passes through a monochromator. The monochromatic output light is collected by the input optical fiber bundle and carried to the integrating cavity assembly. The wavelength of the monochromatic light can be scanned across the wavelength range of interest.

An Oriel 6255 150 W ozone free xenon arc lamp is used as the light source. It has a flat irradiance spectrum from 300 nm to 800 nm. In the infrared region, the spectrum has some peaks and extends to over 2.4 µm. The irradiance begins to drop at wavelengths below 300 nm, but it is still appreciable at 250 nm. The lamp is driven by an Oriel 68700 200 W lamp power supply and is set in an Oriel 66005 lamp housing. A metal coated concave mirror is installed on the back side of the housing to collect light from the lamp and reflect it into the forward direction. The mirror can be adjusted such that the inverted image of the arc lies on the arc itself. A 3 inch diameter f/0.7 Aspherab UV grade fused silica condenser is mounted on the front of the housing to collect the light from the lamp and the back mirror. The focal length is about 52 mm. The condenser produces a collimated beam from the arc with negligible spherical aberration and high efficiency. The collimated beam then passes an Oriel 6214 water filter which is mounted on the condenser and filled with type I pure water. Because of the high absorption of water in the infrared region, undesirable infrared radiation is removed by the filter to reduce the thermal load in the subsequent stages. The filter is cooled by circulating water, which in turn exchanges heat with the cooling water in the building. The beam is then focused by a 3 inch diameter Oriel 41980 plano convex fused silica lens onto the entrance slit of the monochromator. The f/2.6 lens has a focal length of 200 mm at 580 nm.

The light path from the focusing lens of the arc lamp to the entrance of the monochromator is shielded from dust and unintentional obstructions by a piece of black corrugate PVC drainage pipe. The shield also serves to reduce the stray light entering the monochromator entrance slit. A Copal DC-494 plunger shutter with 30 mm diameter is installed in front of the entrance slit of the monochromator. Closing this shutter makes it possible to measure the ICAM background signal due to the photomultiplier dark current and any stray light that might reach the photomultiplier tube. The shutter is powered by a DC 24 V plug-top transformer, which is controlled by an HP 6214A power supply. The shutter defaults to be closed when the power is off.

When measuring the absorption coefficient in the UV, a Schott UG5 glass filter is inserted in front of the monochromator to block visible light and thus reduce the stray light level in the monochromator. The UG5 glass filter has a transmission greater than 80% for the wavelength range 250-390 nm. The transmission is less than 10% for the wavelength range 450-660 nm.

The monochromator is a Digikrom 240 from CVI Laser Corporation. It is a classical Czerny-Turner scanning monochromator with a 240 mm focal length and an effective aperture ratio of f/3.9. The monochromator was upgraded to include UV grade optics inside and a reversible two-grating mount. Both gratings have a 1200 grove/mm ruling, the first has peak transmission at 500 nm and the second at 330 nm. The second one is used when the UV measurements are made. Both gratings give a 3.2 nm/mm reciprocal linear dispersion; therefore a 600 μm slit width will provide a 1.92 nm bandwidth. The monochromator can be controlled either by using a hand held keypad attached to the monochromator by a RS-232C serial port or via an IEEE-488 (GPIB) interface. The primary control of this instrument is by a Macintosh computer running LabVIEW through this GPIB interface; this facilitates automated data collection and analysis.

The input fiber bundle is composed of six silica core silica clad fibers. Each fiber is 1.5 meter long, with a 600 μm core diameter and a 1.0 mm nominal clad diameter. Each fiber is shielded in a protective cable. This custom-made assembly from C Technologies Inc. is used to couple light from the monochromator into the integrating cavity. At the input end the six fibers are arranged in a linear array and embedded in an aluminum ferrule, which is secured in a transparent Plexiglas block by a set screw. The orientation of the linear fiber array with respect to the exit slit, and the distance between the fiber and the exit slit can be adjusted and locked with a set screw. The Plexiglas block is mounted on a Newport X-Y translation stage which is attached to the cover plate in front of the exit slit of the monochromator. This stage is used to adjust the transverse position of the fiber relative to the exit slit. At the output end each fiber terminates in an aluminum ferrule for protection. The output end of each fiber extends about 1.3 cm beyond the ferrule and through a 1 mm I.D. hypodermic tube. All the fiber ends have been polished by Thorlabs polishing films (5 μm film followed by 3 μm then 1 μm films).

The integrating cavity assembly and the output fibers have been discussed in chapter III in detail and will be briefly reviewed here. The integrating cavity assembly is composed of two concentric cylindrical cavities. The outer one is formed by Spectralon; the inner one is formed by fumed silica packed between the sample cell and a fused silica tube. Six input fibers carry light collected from monochromator into the outer cavity to provide uniform illumination of the sample stored in the inner cavity. The outward irradiances of the cavities are sampled by two output fibers. These two output fibers carry light to the light chopper box.

3. Detecting components

The chopper is a Model 197 precision light chopper from EG&G Princeton Applied Research. This extremely compact unit comprises the dual aperture chopper disc, motor and necessary driving electronics. The head contains all the control circuitry to keep the chopper blade synchronized to its own internal precision oscillator or to an external frequency signal. The unit is powered by an HP 6235A power supply. There are two sets of apertures on the chopper disc. The outer 30 apertures cover the frequency range 150-3000 Hz and the inner 3 apertures cover the frequency range 15-300 Hz. Once the frequency f is set to a specific value using the 4 digit pushbutton frequency selector, the light going through the outer apertures is chopped at frequency *f* and the light going through the inner aperture is chopped at frequency *f/10*. The unit has two synchronous square wave outputs with 10 V nominal peak to peak values. One of the two outputs has a frequency *f*, the other *f/10*. These two synchronous signals are fed to two lock-in amplifiers as references. The whole unit comes in the form of a black box with two windows on the front and back sides of the chopper disc, just opposite each other. If the output fibers from the integrating cavity assembly are mounted on one window and a photomultiplier tube (PMT) mounted on the other, no stray light from outside the box can reach the PMT, thus background noise is minimized.

For wavelengths below ~300 nm, the signal is weak and minimizing noise is essential. All noise sources were identified and eliminated. In the chopper box, two light emitting diodes (LED) are used to facilitate measuring the chopper speed. The two LEDs emit infrared light at around 900 nm. The infrared light bounces around in the box, gets modulated by the chopper and finds its way to the PMT through the window, producing a significant amount of background signal. To remove this background signal, the fiber coupling assembly as shown in Fig. 5.2 is used. The output fibers from the integrating cavity assembly are fixed on an aluminum block. The aluminum block is then mounted on the chopper box in such a way that the ends of the fibers are very close to the chopper blade and each fiber pointing to either outer aperture or inner aperture, respectively. On the other side, two short pieces of optical fibers with larger diameter are mounted in the same way. These two fibers are Thorlabs BFH37-1500 multimode fibers with a 1.5 mm core diameter. The two pairs of fibers are aligned to each other such that the short pieces of fibers efficiently accept the light from the output fibers. The PMT housing is attached to the aluminum block on which the short fibers are fixed. The only way light can get to the PMT is through the two short fibers. In this design, signal light is transmitted with little loss while the background light transmission is minimized. This significantly increased the signal noise ratio (SNR).

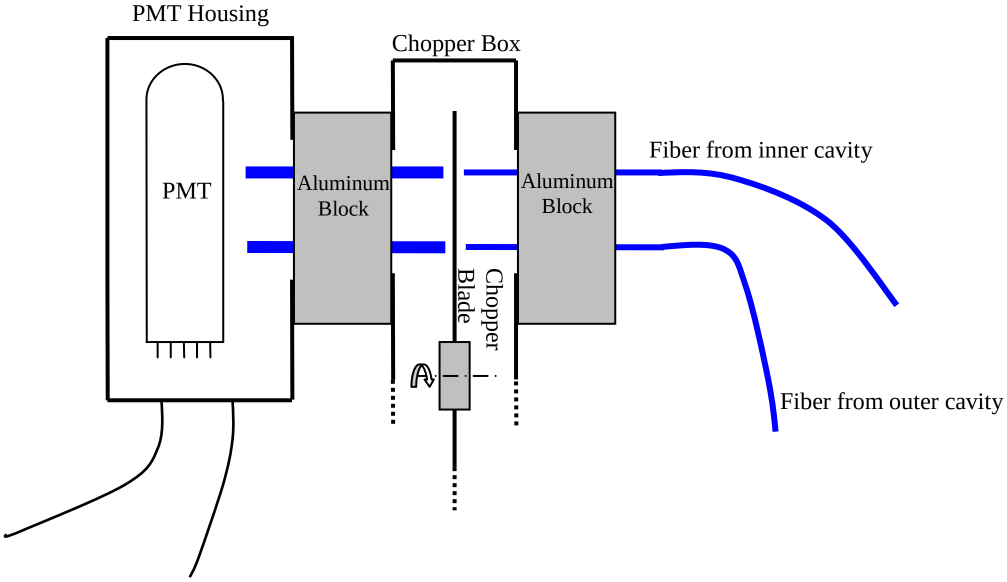

Fig. 5.2. Fiber coupling assembly mounted on chopper box.

To further reduce the effect of the 900 nm LED, the detector was a Hamamatsu R1527 PMT that is specified for the wavelength range 185-680 nm; its spectral response drops quickly at wavelengths longer than 680 nm. It has a peak anode sensitivity of 4.0×10^5 A/W at 400 nm. Anode dark current is typically 0.1 nA. The PMT is enclosed in a magnetic shield that is connected to the electrical ground; it is set inside a housing together with the resistor voltage divider. The PMT is operated with 1100 V DC applied across the voltage divider; its output is terminated by a 4.6 MΩ resistor. A BNC cable carries the output signal S_{mix} to the lock-in amplifiers. This signal S_{mix} includes the information from both the outer and inner cavities. Because they were chopped at two different frequencies, the information can be extracted by two lock-in amplifiers.

One lock-in amplifier is a Model 5210 from EG&G Instruments, the other is a Model SR830 from Stanford Research Systems. In our setup, light from the inner cavity is chopped by the outer aperture with frequency *f*. The synchronous signal with frequency *f* from the light chopper box is fed to the SR830. Thus, the SR830 provides the inner cavity signal S_0. Similarly, the EG&G 5210 produces the outer cavity signal S_1 using the synchronous signal at frequency *f/10*. These two values, S_0 and S_1, are read by the computer through the GPIB interfaces on the back of the lock-in amplifiers.

An oscilloscope can be used to monitor the signal S_{mix} from the PMT. But when data is being taken, the oscilloscope is detached to avoid loading by the scope input resistance.

4. Software

A Macintosh Quadra 840AV equipped with a National Instruments IEEE-488 controller is used to control the equipment and obtain data from the equipment for further processing. The monochromator and the two lock-in amplifiers are connected to the computer via GPIB cables. The data acquisition, instrument control, and signal processing are accomplished using the LabVIEW programming language from National Instruments. LabVIEW is a graphical programming language with many built in functions for instrument control and data analysis. In LabVIEW, the programmer creates a virtual instrument (VI) which consists of a front panel and a block diagram. The front panel is the user interface, providing the input and output parameters for the program. The block diagram contains the actual programming "code" that uses a combination of built in functions and custom functions. Because of the popularity of LabVIEW, some manufacturers provide custom LabVIEW programs along with their instruments. Consequently, the user only needs to use those custom designed programs as sub-programs to perform the basic operations of the instrument. For example, the monochromator used in this experiment came with a set of programs for adjusting the wavelength, setting the slit width, and acquiring the equipment information etc.

In our LabVIEW program, we send commands to the monochromator to adjust the slit width and set the initial wavelength. We then wait for the lock-in amplifiers to settle down before reading the values S_0 and S_1. S is then calculated from S_1/S_0. All this information is written to a text file. The wavelength is then changed by some predetermined step and all of the above is repeated. Steps in the wavelength are repeated until the final wavelength in the desired range is reached.

The resulting text file containing the wavelengths and the signal S is then processed by MATLAB programs to give the final results for the absorption coefficients.

CHAPTER VI

EXPERIMENT RESULTS

1. Preliminary tests

Although the Xenon light source produces broad band spectrum radiation, the illumination system has a low throughput at wavelengths less than 300 nm. Careful alignment of the optics must be done to optimize the throughput in the UV region. After alignment, the output power of the monochromator at the exit slit is measured. The result is shown in Fig. 6.1. The entrance and exit slit widths are set at 600 µm. The total output power of three (out of six) input fibers is also measured and shown in Fig. 6.2.

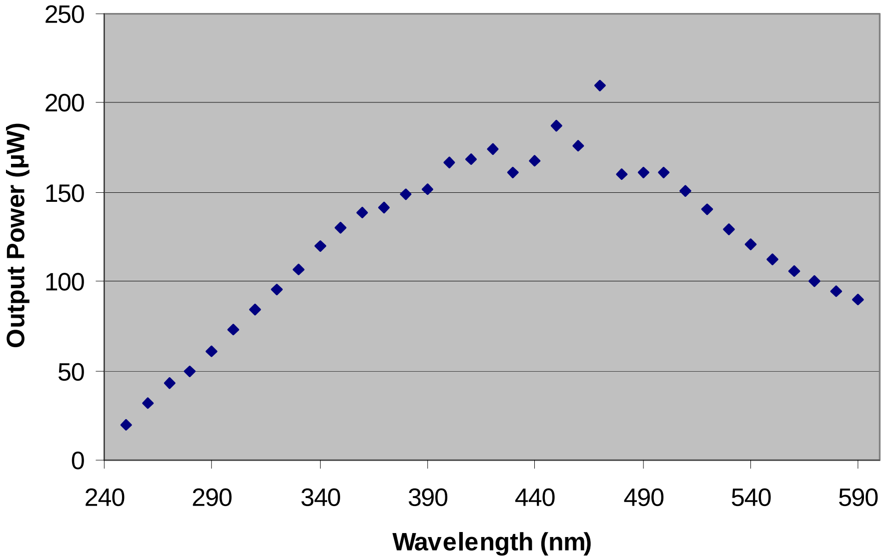

Fig. 6.1. Output power right after the monochromator exit slit.

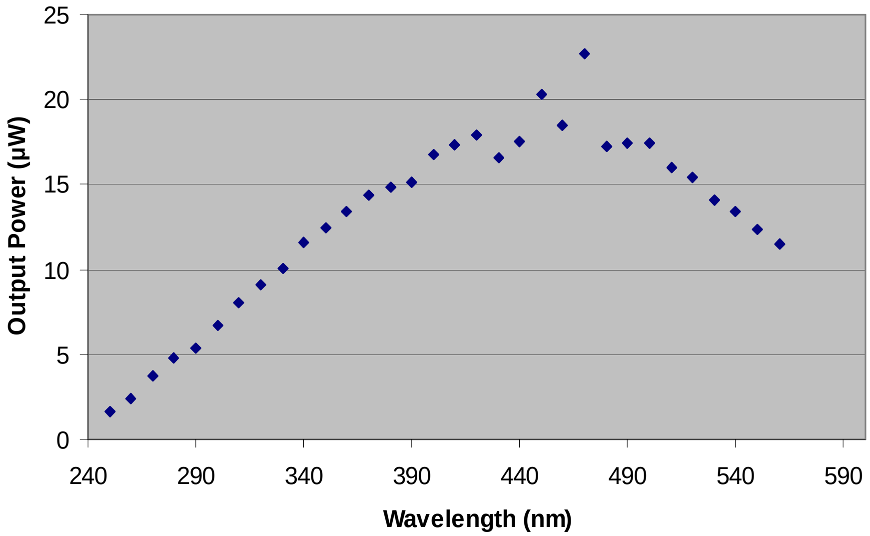

Fig. 6.2. Total output power of three input fibers.

The integrating cavity assembly, output fibers and the PMT are enclosed in a small dark space made of light shielding cloth. Almost all environmental light is blocked by the shield. When data is being taken, the room light is also turned off to minimize environmental light. The background signal is measured by closing the shutter in front of the monochromator and reading the two lock-in amplifiers. When the shutter is closed, no light from the arc lamp enters the cavities. Under these conditions, the reading from the inner cavity is less than 5 μV; from the outer cavity is less than 2 μV. Fluctuations of the background signal are of the same magnitude. Compared to the signals we are measuring, which are at least 2 mV in magnitude, this background can be ignored. These background measurements were made when the room is in a complete darkness. But even when the room light is turned on, the outer cavity signal is less than 100 μV and the inner cavity signal is about 1 mV. The inner cavity signal is mainly due to the light guided by the quartz tubes directly into the inner cavity. Shielding the tubes is important to minimize the environmental light background and noise. Without the shielding, cavity signals easily saturate the lock-in amplifiers.

The time dependence of the signal during the equipment warm-up was investigated in [39, 42]. To minimize warm-up effect, all the equipment was left on during periods of data acquisition; this avoided the need to wait about two hours every day for the equipment to warm up. Every round of data acquisition usually took about one or two days. Consequently, it was necessary to investigate the possible leaching of contaminants from the wall of the sample cell. In previous studies, the absorption was found to increase if the pure water sample was left in the sample cell for an extended time, probably due to the contaminants from the cell wall. To investigate this effect in our new cavity, we left the pure water sample in the sample cell and measured the full cavity signal at a wavelength of 300 nm every 30 seconds for 232240 seconds (64.5 hours). The result is shown in Fig. 6.3 and Fig. 6.4 shows the histogram. The average of the data is 1.80 and the standard deviation is 0.02. During the 64.5 hours, we didn’t see any significant change of the full cavity signal except the statistical noise. This is because the material chosen for the sample cell is the purest optical material. The Heraeus Suprasil synthetic fused silica is manufactured by flame hydrolysis to extremely high standards. The resultant material has an impurity content of only about one part per million. Thus the contaminants coming off the sample cell wall are negligible and don't have an observable effect on the signal.

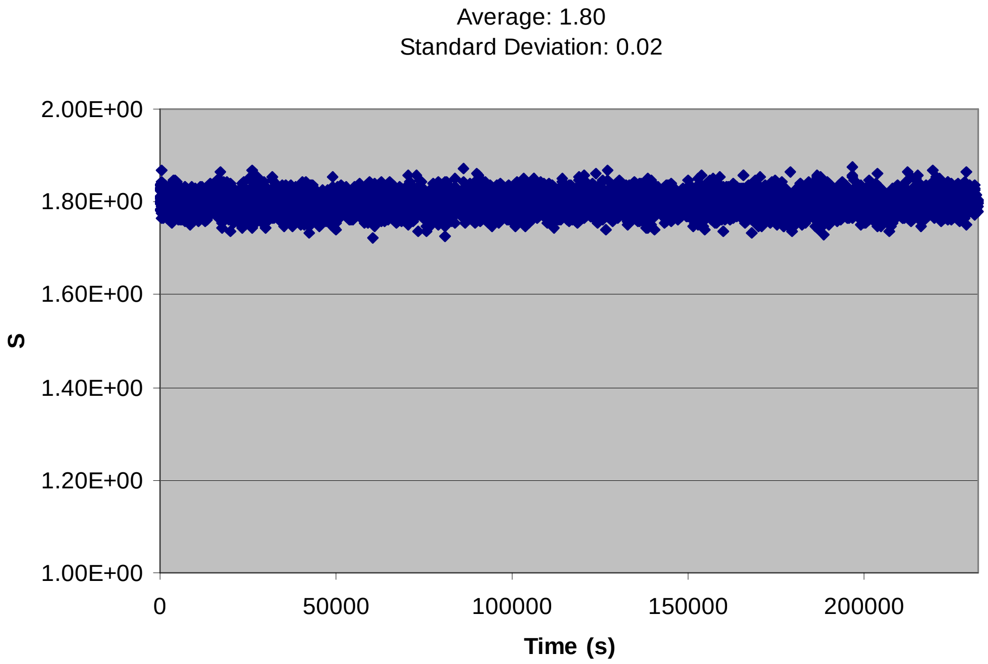

Fig. 6.3. Signal dependence on the time that the sample is left in the cell. (Wavelength at 300 nm)

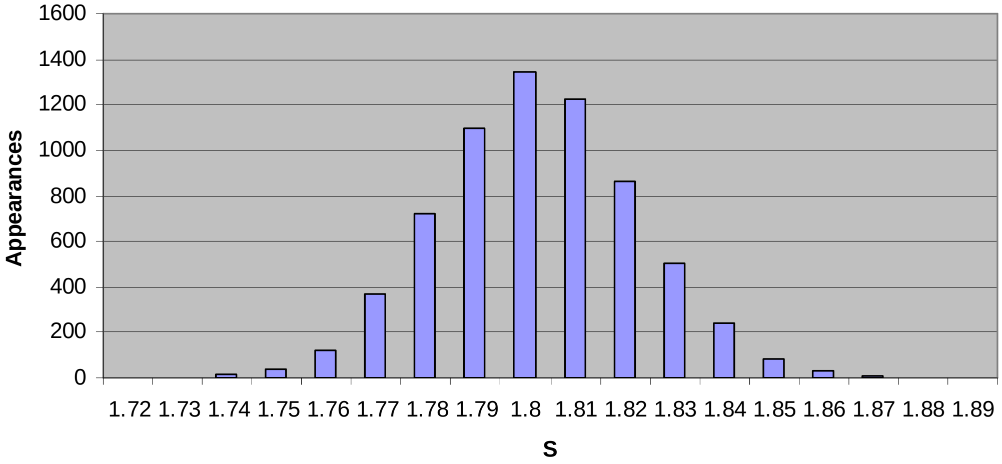

Fig. 6.4. Histogram of the signal measured over time.

2. Calibration

In chapter II, we have obtained the relationship between the sample absorption coefficient and the slope of the signal versus volume, equation 2.17. We write it down again here as our basic working equation

$$\left.\frac{\partial S}{\partial V}\right|_a = \frac{a}{C_1}, \tag{6.1}$$

where we have omitted the explicit factor 4; it is included in the calibration constant C_1. It should be noted that this relationship is true not only for pure water, but also for any liquid medium. To obtain the slope, the volume of the sample in the sample cell is varied and the corresponding signal is measured. The slope information is then obtained via a least square fit to a straight line. A typical set of data is shown in Fig. 6.5. The slope *p*, i.e. $\partial S/\partial V$, for this set of data is 0.0032. The volumes are chosen from 50 mL to 550 mL in intervals of 50 mL. We avoid choosing 0 mL and full cavity, because nonlinearity effects occur at these two extremes in volume [39, 42].

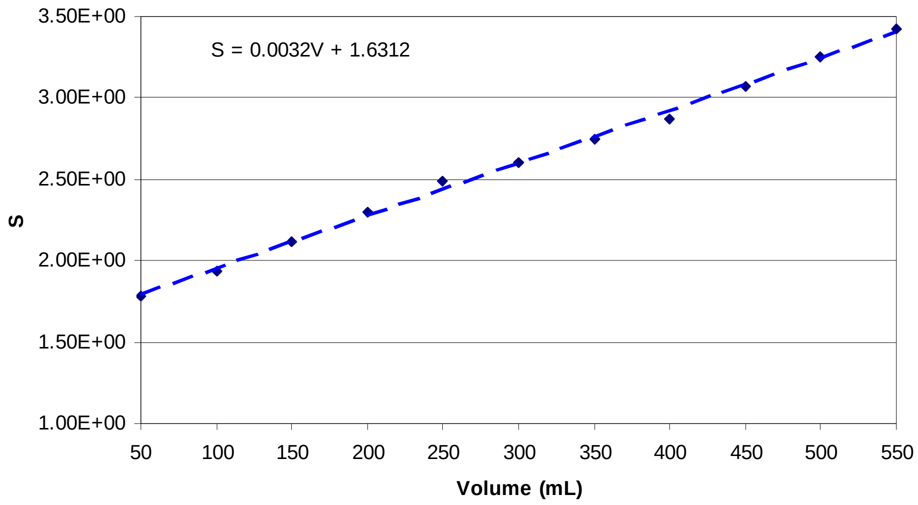

Fig. 6.5. A typical set of signal versus volume data. The blue line is determined by least square fitting.

If we only make measurements on the pure water sample, we don't have enough information to determine the absorption coefficient because we don't know C_1. C_1 is a calibration parameter depending on so many characteristics of the ICAM that it can only be accurately determined by experiment. We determine values of C_1 at each wavelength using the following calibration procedure; the absorption coefficient of pure water is determined at the same time.

If we have a solution for which we already know the absorption coefficient $a_{solution}$, we can obtain the slope information for the solution in the same way as for pure water. Specifically we have

$$p_1 = \frac{a_{water}}{C_1} \tag{6.2}$$

and $$p_2 = \frac{a_{solution}}{C_1}, \tag{6.3}$$

where p_1 is the slope for pure water and p_2 is the slope for the solution; both have been determined from the experimental data.

However, for a solution of a solute in a solvent (water in our case) we take the total absorption of the sample to be the superposition of the absorption values of its constituents. That is

$$a_{solution} = a_{water} + a_{solute}. \tag{6.4}$$

In our experiment, we choose Irgalan Black, a dye powder, as the solute and pure water as solvent. We first prepare a master dye solution by dissolving about 50 milligrams of the Irgalan Black dye powder in 250 mL of type I pure water. The ultrasonic bath was used to break up the dye particles and facilitate the dissolving process. We then filter out the leftover un-dissolved particles using Fisherbrand P5 filter paper and dilute the solution to a 2 L volume. The absorption of this solution is measured using a Spectramax Plus^{384} spectrophotometer. Spectramax Plus^{384} provides a measurement of the optical absorbance of a sample solution in a quartz cuvette with 10 mm light path length. It has a wavelength range of 190-1000nm, an absorbance measuring range of 0.0-4.0, and an accuracy of better than ±0.005. The dimensionless optical absorbance is defined as

$$A = \log_{10}(I_0 / I)\,, \tag{6.5}$$

where I_0 is the incident light intensity and I is the transmitted light intensity.

In measuring the absorbance, the light loss during passing through the cuvette includes the reflection off the air quartz interfaces and the water quartz interfaces, pure water absorption and dye absorption. The spectrophotometer itself cannot differentiate the losses due to these different mechanisms. To obtain only the dye absorption, we must remove the effects of reflections and pure water absorption. Consequently, we measure the absorbance with only pure water in the cuvette to obtain absorbance A_1, then again with the dye solution in the cuvette to obtain absorbance A_2. By definition, the following relationships hold for the two absorbances A_1 and A_2:

$$I_1 = I_0(1-R)10^{-A_{water}} = I_0 10^{-A_{water}-A_{reflection}} = I_0 10^{-A_1} \tag{6.6}$$

$$I_2 = I_0(1-R)10^{-A_{water}-A_{dye}} = I_0 10^{-A_{water}-A_{reflection}-A_{dye}} = I_0 10^{-A_2}\,, \tag{6.7}$$

where R is the total reflection loss, $A_{reflection}$ equals to $-\log_{10}(1-R)$ and we have used equation 6.4 for the absorbance of a solution. The absorbance caused by only the dye solute A_{dye} is then the difference between these two measured absorbances: $A_{dye} = A_2 - A_1$. Using this procedure, we measured the dye absorbance over the wavelength range, 250 nm to 700 nm in 1 nm intervals. The partial set of these results from 250 nm to 400 nm in 5 nm intervals is tabulated in table 6.1. It should be noted that the absorbance and the absorption coefficient have different meanings. The absorbance measures the total loss of the sample regardless of its length, and thus is a dimensionless quantity. The absorption coefficient measures the loss per unit length, and has a unit of m^{-1}. Comparing the definition of absorbance and the definition of the absorption coefficient used in the thesis, we obtain the relationship as

$$a_{MasterDye} = \frac{1}{L}\ln\frac{I_0}{I} = \frac{\ln 10}{L}\log_{10}\frac{I_0}{I} = 2.303\frac{A_{dye}}{L} \qquad (6.8)$$

where L is the path length through the sample; L is 10 mm for the quartz cuvette used in Spectramax Plus^{384}. After converting the absorbance to the absorption coefficient, we have results shown in Fig. 6.6.

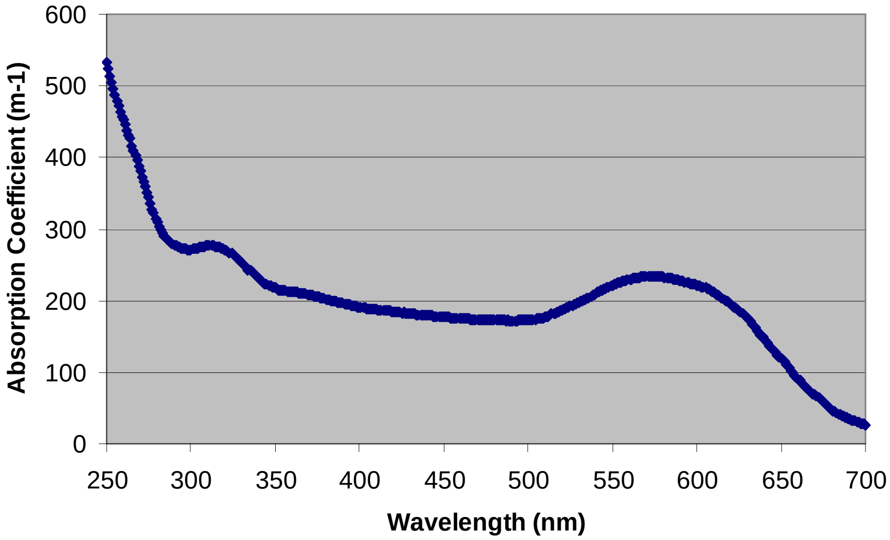

Fig. 6.6. Absorption coefficient of master Irgalan Black dye.

Table. 6.1. Absorption coefficient of master Irgalan Black dye from 250 nm to 400 nm in 5 nm intervals, measured with Spectramax Plus^{384}. (The sample is contained in quartz cuvette with 10 mm path length.)

Wavelength (nm)	Absorption (m^{-1})	Wavelength (nm)	Absorption (m^{-1})
250	532.52	330	253.01
255	486.72	335	241.63
260	452.33	340	231.84
265	416.38	345	222.77
270	381.56	350	218.51
275	343.35	355	213.60
280	308.67	360	211.99
285	288.54	365	210.29
290	277.95	370	208.35
295	273.02	375	205.24
300	271.78	380	202.00
305	274.68	385	199.05
310	276.34	390	196.63
315	275.58	395	193.59
320	271.73	400	190.85
325	264.25		

This master dye solution cannot be used for calibration, because the absorption coefficient is too large. Since we want to measure pure water absorption coefficients on the order of 0.01~0.1 m^{-1}, we prefer calibration solutions to have about the same order of magnitude. We can do this by diluting the master dye solution precisely with type I pure water, using volumetric pipettes and flasks. After diluting the master dye solution by 800 times, we get a solution with an absorption coefficient $a_{solution}$ composed of both solute and solvent, i.e. dye and pure water as

$$a_{solution} = \frac{a_{MasterDye}}{Dilution} + a_{water} = a_{dye} + a_{water} \, . \tag{6.9}$$

Combining equations 6.2, 6.3 and 6.9, we obtain

$$C_1 = \frac{1}{p_2 - p_1} a_{dye} \tag{6.10}$$

where p_1 and p_2 are slopes for pure water and dye solution, respectively, extracted from experiment data, and a_{dye} is calculated from the master dye absorption coefficient divided by the dilution factor. The pure water absorption is then given by

$$a_{water} = \frac{p_1}{p_2 - p_1} a_{dye} \tag{6.11}$$

3. Error analysis

From equations 6.10 and 6.11, it's easy to see that errors in a_{water} and C_1 can only come from the errors in quantities p_1, p_2 and a_{dye}. The error in a_{dye} comes from the absorbance measurement and the dilution process. The smallest absorbance value measured for the master dye solution in the wavelength range of 250 nm to 400 nm is 0.829 (at 400 nm). The accuracy of Spectramax Plus^{384} is $< \pm 0.005$. So the relative accuracy is $< \pm 0.6\%$. We first diluted the master dye solution by a factor of 20, and then diluted this second solution again by a factor of 40 to make a total dilution factor of 800. When diluting, we have used a volumetric pipette with volume 25 mL and an accuracy of ±0.03 mL and a volumetric flask with volume 1 L and an accuracy of ±0.3 mL. The relative accuracies are ±0.1% and ±0.03% respectively. The total relative accuracy of the diluted dye solution is then less than ±1% roughly, which is much less than the uncertainties in p_1 and p_2. Consequently, we will ignore the uncertainty in a_{dye} in the following data analysis.

Consider the uncertainties in p_1 and p_2. Suppose there are N pairs of measurements $(S_1, V_1), (S_2, V_2), \ldots, (S_N, V_N)$, to fit to the following linear function via a least square fit [44]

$$S = pV + c\,, \tag{6.12}$$

where p is the slope and c is the intercept with S axis, see Fig. 6.5. Then p and c are given by

$$\begin{aligned} p &= \frac{N\sum VS - \sum V \sum S}{\Delta} \\ c &= \frac{\sum V^2 \sum S - \sum V \sum VS}{\Delta} \end{aligned}\,, \tag{6.13}$$

where

$$\Delta = N\sum V^2 - \left(\sum V\right)^2\,. \tag{6.14}$$

All the sums are on the index i, which ranges from 1 to N. Because of the statistical error in the measurement results, there are uncertainties in p and c. The uncertainties are given by

$$\begin{aligned} \sigma_p &= \sigma_S \sqrt{\frac{N}{\Delta}} \\ \sigma_c &= \sigma_S \sqrt{\frac{\sum V^2}{\Delta}} \end{aligned}\,, \tag{6.15}$$

where

$$\sigma_S = \sqrt{\frac{1}{N-2}\sum (S_i - pV_i - c)^2}\,, \tag{6.16}$$

with p and c given in equation 6.13.

The uncertainties in p_1 and p_2 will propagate into the uncertainty of the water absorption coefficient a_{water}, and this uncertainty can be calculated as

$$\sigma_a = \sqrt{(\partial a/\partial p_1)^2 \sigma_{p_1}^2 + (\partial a/\partial p_2)^2 \sigma_{p_2}^2} \ . \tag{6.17}$$

From equation 6.11, we have

$$\begin{aligned} \frac{\partial a}{\partial p_1} &= \frac{p_2}{(p_2 - p_1)^2} a_{dye} \\ \frac{\partial a}{\partial p_2} &= -\frac{p_1}{(p_2 - p_1)^2} a_{dye} \end{aligned} \ . \tag{6.18}$$

Similarly, the uncertainty in the calibration parameter C_1 can also be calculated as

$$\sigma_{C_1} = \sqrt{(\partial C_1/\partial p_1)^2 \sigma_{p_1}^2 + (\partial C_1/\partial p_2)^2 \sigma_{p_2}^2} \ , \tag{6.19}$$

where, from equation 6.10,

$$\begin{aligned} \frac{\partial C_1}{\partial p_1} &= \frac{1}{(p_2 - p_1)^2} a_{dye} \\ \frac{\partial C_1}{\partial p_2} &= -\frac{1}{(p_2 - p_1)^2} a_{dye} \end{aligned} \ . \tag{6.20}$$

4. Results

Fig. 6.7 shows the ICAM signal *S* as the function of the volume *V* of the pure water sample at different wavelengths. The linear least square fit is the straight line in each plot. The slope of the fitted line and its standard deviation is shown in the plot for each wavelength. Fig. 6.8 shows the ICAM signal *S* as the function of the volume *V* of the dye solution at the same set of wavelengths. The dye solution is diluted from the master dye solution by a factor of 800 using precise volumetric pipettes and volumetric flasks.

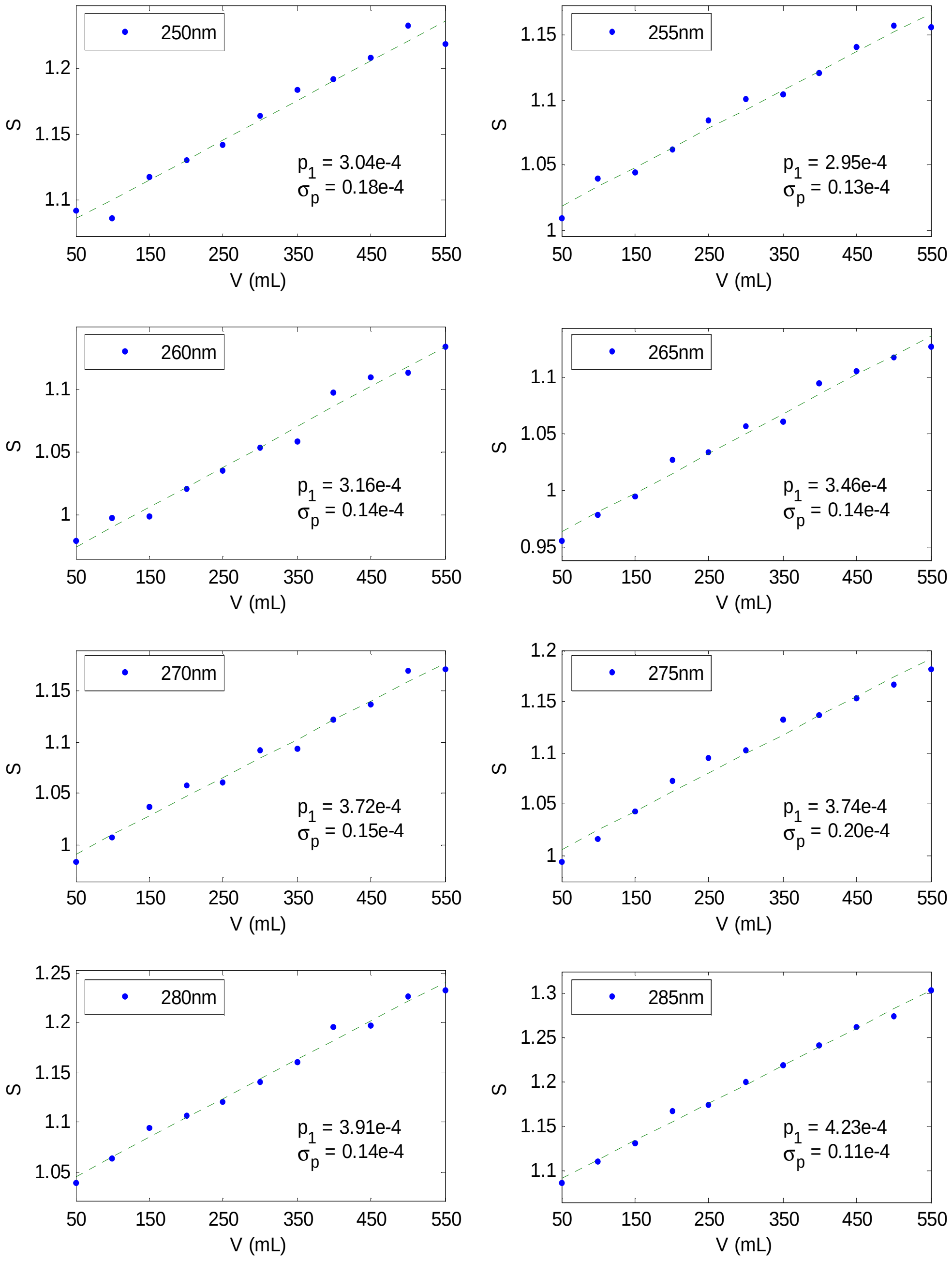

Fig. 6.7. The signal *S* as a function of the pure water volume *V* at different wavelengths, as well as the linear fitting line. The slopes and the standard deviations of the slopes are shown.

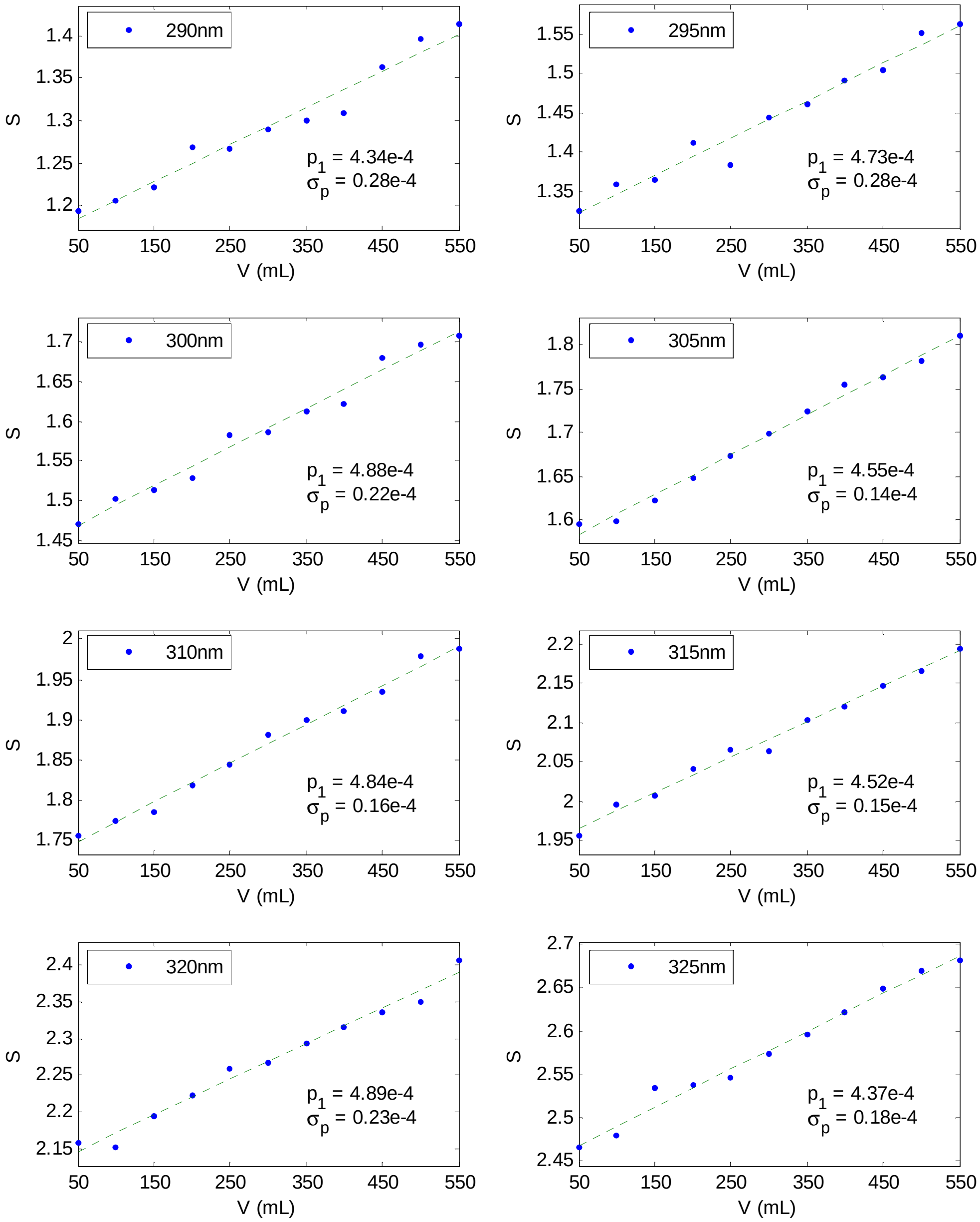

Fig. 6.7. Continued.

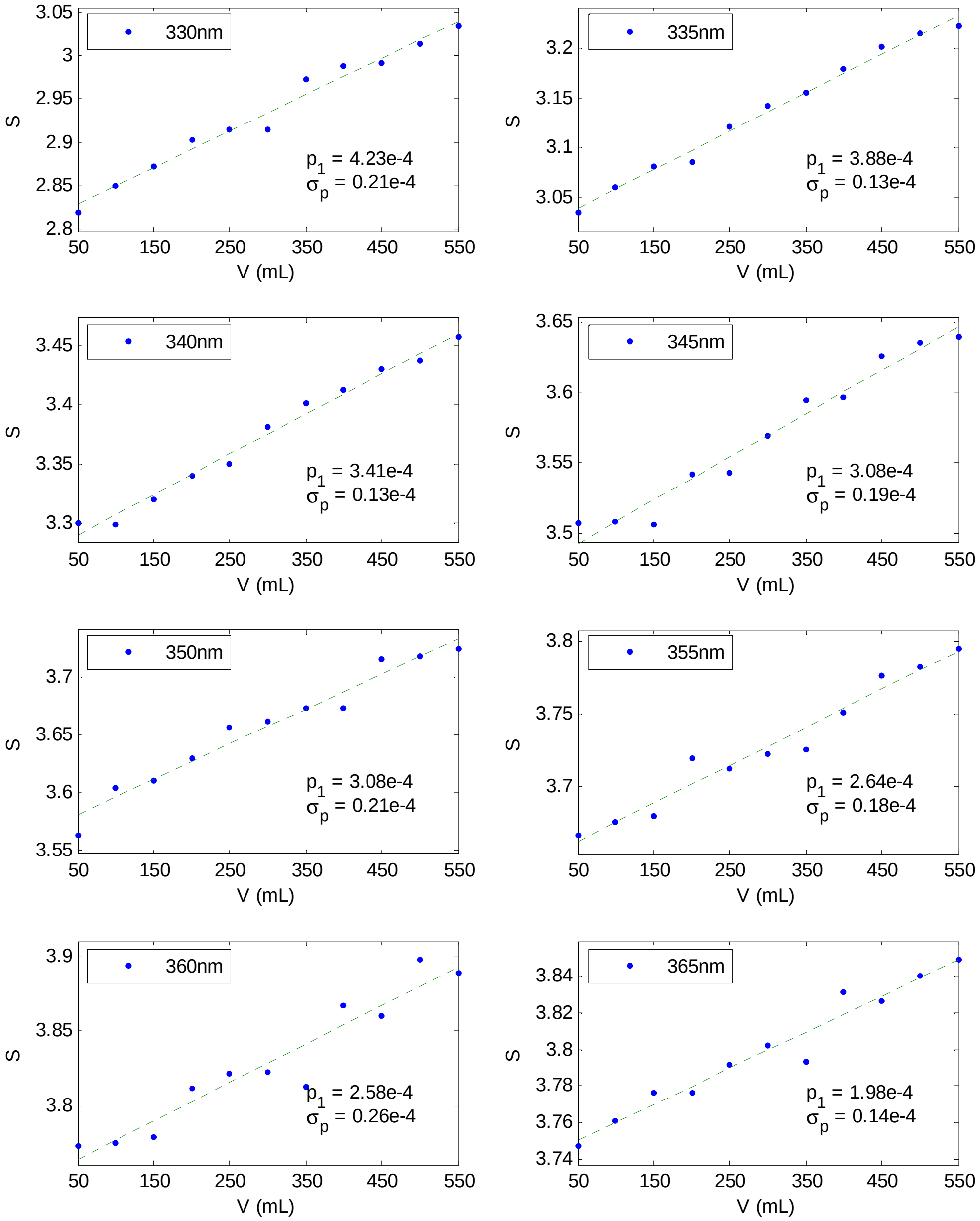

Fig. 6.7. Continued.

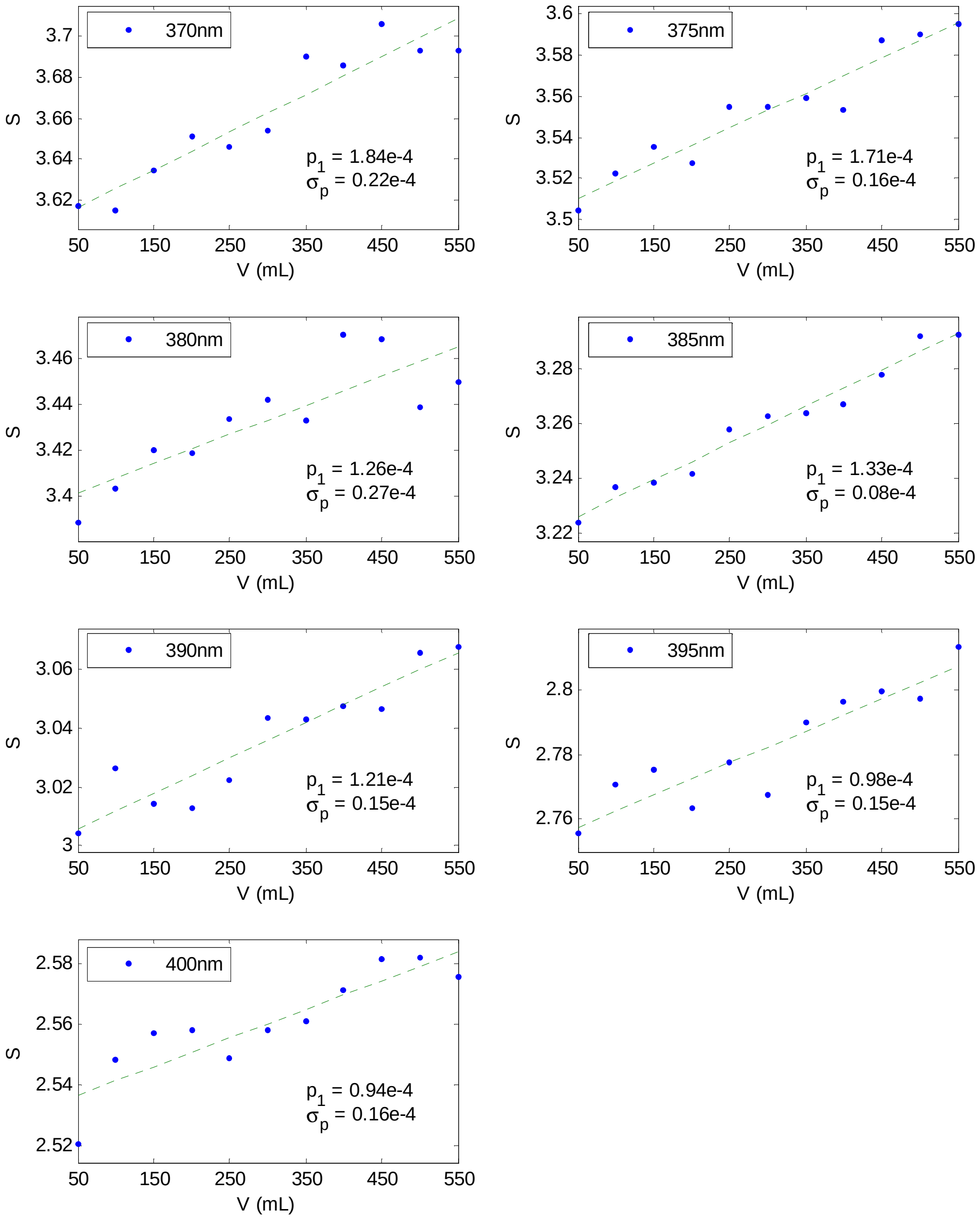

Fig. 6.7. Continued.

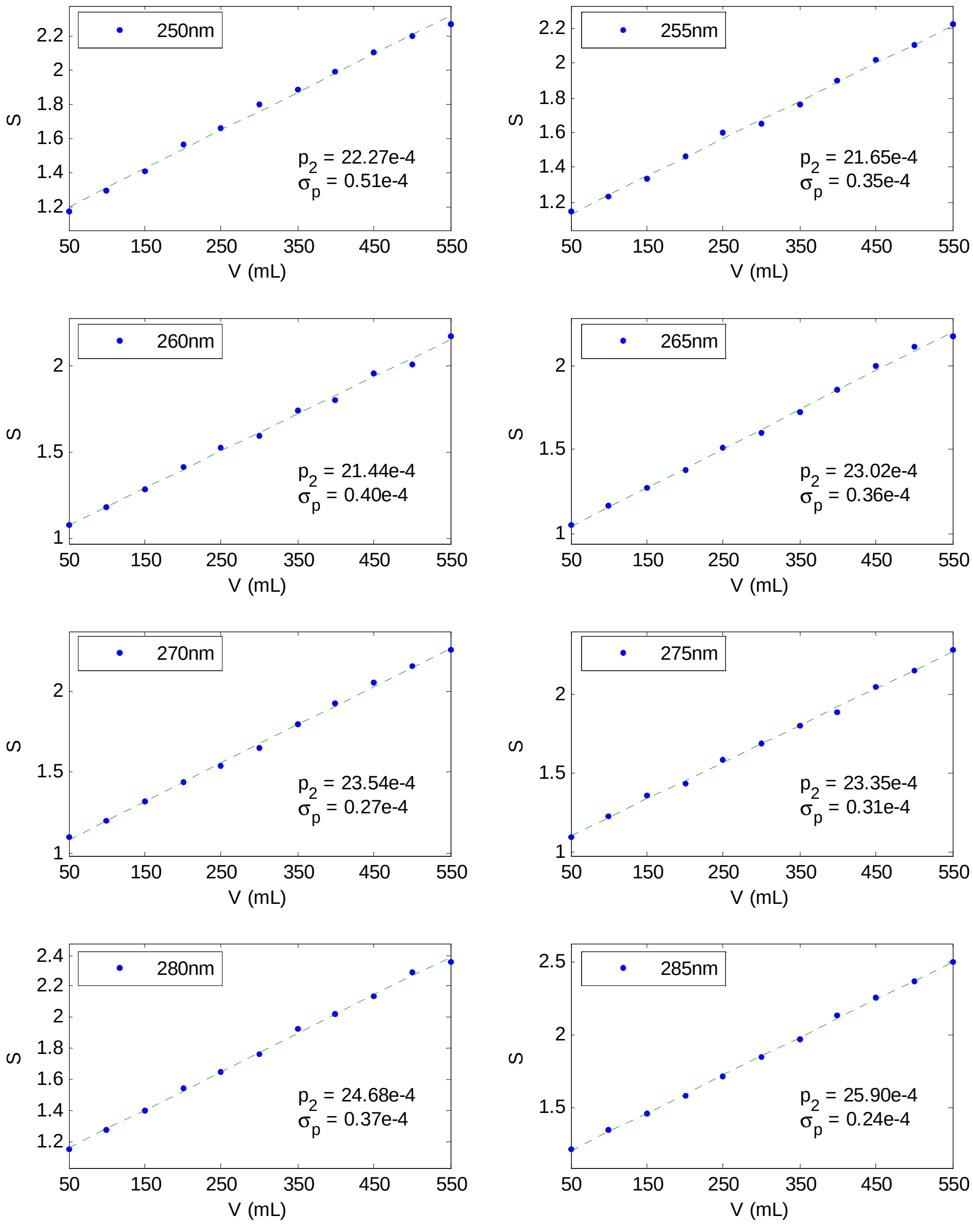

Fig. 6.8. The signal *S* as a function of the dye solution volume *V* at different wavelengths, as well as the linear fitting line. The dye solution is diluted from master dye solution by a factor of 800. The slopes and the standard deviations of the slopes are shown.

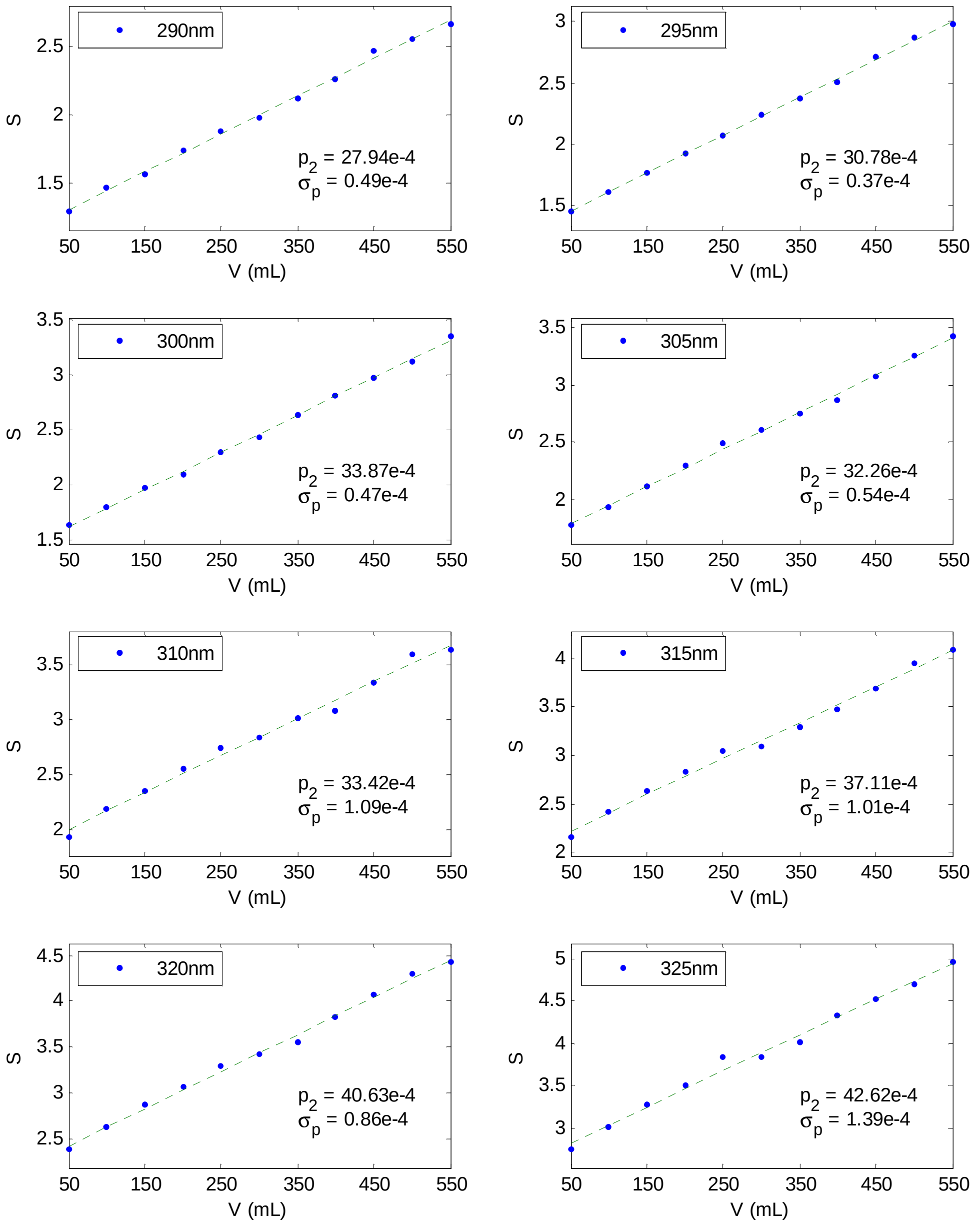

Fig. 6.8. Continued.

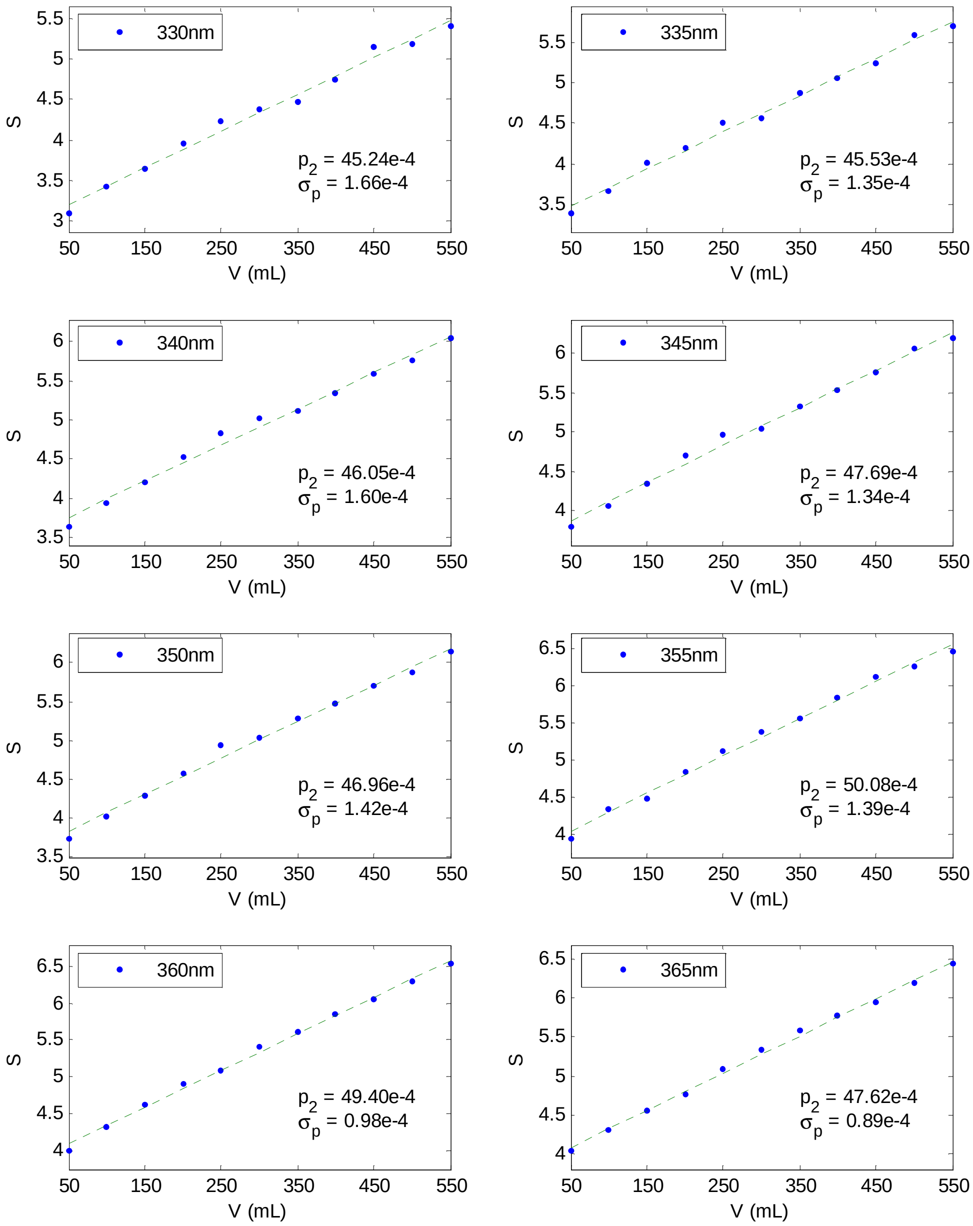

Fig. 6.8. Continued.

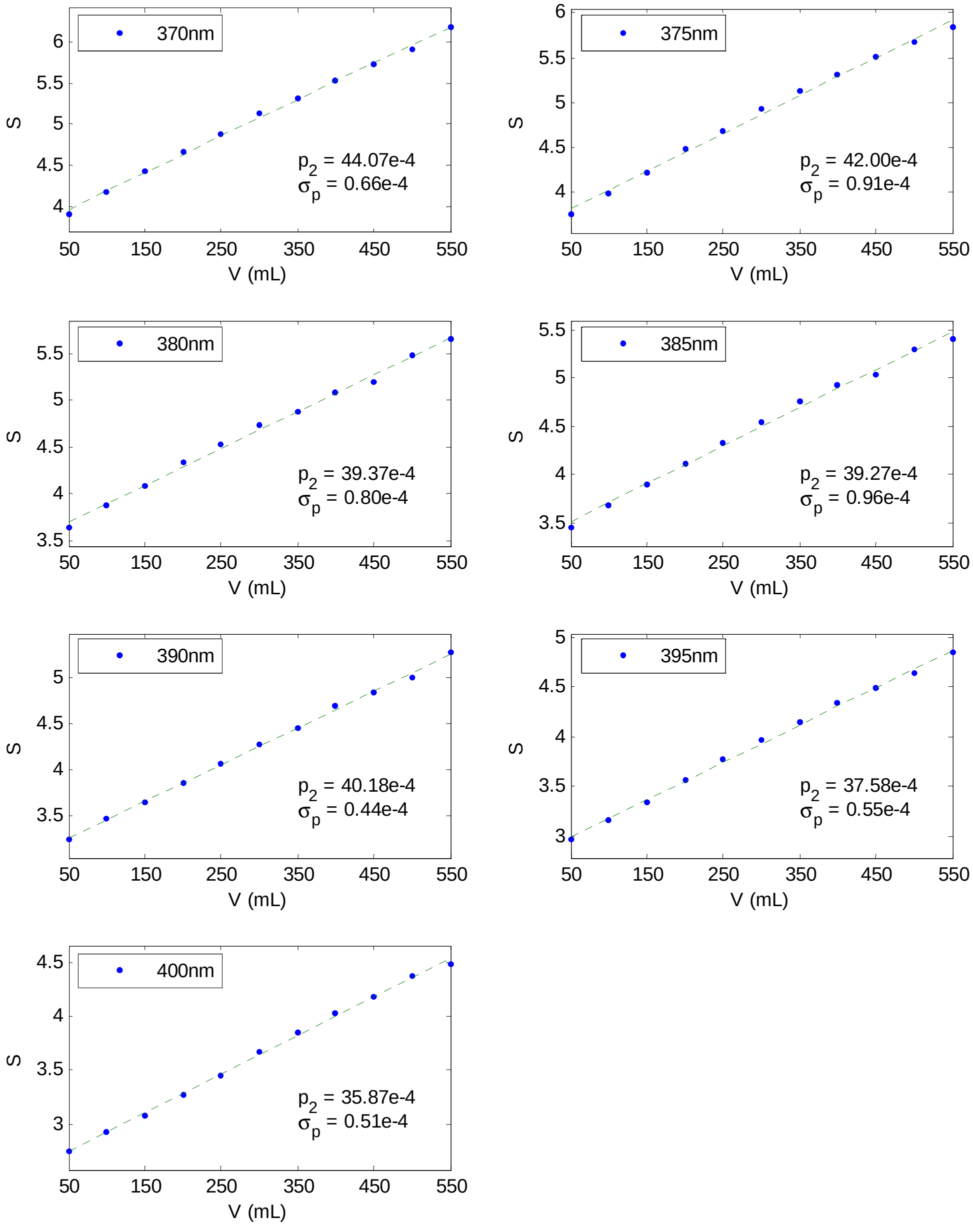

Fig. 6.8. Continued.

The resulting optical absorption coefficients and the corresponding uncertainties of pure water at wavelengths from 250 nm to 400 nm, in 5 nm intervals, are given in table 6.2. The results were averaged over three measurements.

Table 6.2. The optical absorption coefficients of pure water at wavelengths from 250 nm to 400 nm, in 5 nm intervals. (Average of three measurements)

Wavelength (nm)	Absorption Coefficient (m^{-1})	Standard Deviation (m^{-1})	Percentage (%)
250	0.1036	0.0057	5
255	0.0957	0.0035	4
260	0.1023	0.0030	3
265	0.0950	0.0024	3
270	0.0913	0.0022	2
275	0.0848	0.0025	3
280	0.0747	0.0015	2
285	0.0704	0.0013	2
290	0.0621	0.0027	4
295	0.0595	0.0021	3
300	0.0552	0.0014	3
305	0.0576	0.0017	3
310	0.0516	0.0015	3
315	0.0488	0.0014	3
320	0.0448	0.0012	3
325	0.0373	0.0014	4
330	0.0329	0.0012	4
335	0.02790	0.00086	3
340	0.02223	0.00075	3
345	0.01834	0.00061	3
350	0.01650	0.00072	4
355	0.01517	0.00072	5
360	0.01408	0.00072	5
365	0.01208	0.00060	5
370	0.01144	0.00073	6
375	0.01161	0.00068	6
380	0.00928	0.00097	10
385	0.00836	0.00045	5
390	0.00713	0.00053	7
395	0.00659	0.00059	9
400	0.00655	0.00059	9

Fig. 6.9 shows the absorption coefficients at wavelengths from 250 nm to 400 nm from the present work, together with Pope & Fry's data from 380 nm to 600 nm [28], Quickenden & Irvin's data from 200 nm to 320 nm [17], Litjens, Quickenden & Freeman's data [19] from 300 nm to 600 nm and Lu & Fry's data from 300 nm to 400 nm [39].

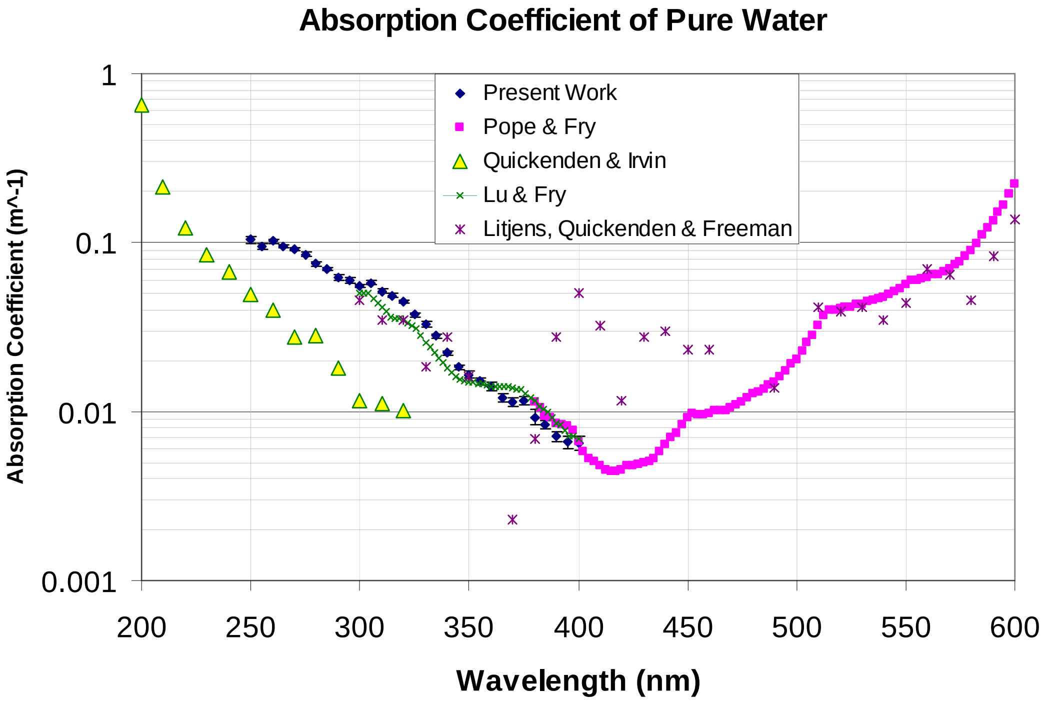

Fig. 6.9. The optical absorption coefficients of pure water, including the data from present work, Pope & Fry's data, Quickenden & Irvin's data, Litjens, Quickenden & Freeman's data and Lu & Fry's data.

At wavelengths between 380 nm and 400 nm, our present work shows good agreement with the data of Pope and Fry. It should be noted that these two independent measurements used two different reflective materials for the integrating cavity: Spectralon and fumed silica. In addition, a new pure water system was installed, most optical elements have been changed for UV compatibility, and new signal detection system was implemented. The agreement between these two measurements has proved the robustness of the ICAM concept and its usefulness in measuring the absorption coefficient of a liquid medium with small absorption.

At wavelengths between 300 nm and 400 nm, our new data is slightly higher than Lu & Fry's data from earlier measurements. Since their data has large uncertainty at this region, the two measurements agree well.

At wavelengths between 250 nm and 320 nm, our data is higher than Quickenden & Irvin's data. They attributed their low absorption coefficient to their exceptional high water purity that was prepared in their lab. But their later measurement, Litjens, Quickenden & Freeman's data, on the pure water prepared in exactly the same way, showed more similarity to our data at wavelengths between 300 nm and 400 nm than to their earlier measurements. Taking uncertainty into account, Litjens, Quickenden and Freeman's data agrees well with our data in this region.

Our measurements have a higher uncertainty at wavelengths between 350 nm and 400 nm. Basically, the sensitivity of the ICAM design used in this work is not high enough for the low absorption in this region. The sensitivity of the ICAM is determined by the total effective path length, which in turn is determined by two factors: the physical size of the cavity and the reflectivity of the cavity wall. The reflectivity of the ICAM wall, made of fumed silica in our current design, depends mainly on the thickness of the wall. Our current ICAM has an inner cavity wall thickness of 5 mm. Spectralon used in our current ICAM also limits the sensitivity in the UV region because of its relatively lower reflectivity in this region. We have designed a new version of the ICAM that is larger in size, having a thicker inner cavity wall and made entirely of high purity silica. Fig. 6.10 shows the new design. The sample cell, part A, has a 1.7 L capacity, about 3 times the current ICAM's capacity of 0.6 L. Parts A, B, C, D, E, F and G are made of Suprasil synthetic fused silica from Heraeus, which has the lowest absorption in the visible and near UV among all commercial optical materials. The gray area is filled with fumed silica. The thickness of the inner cavity wall is about 10 mm, twice the thickness of the current ICAM. Thus, the new ICAM is expected to be much more sensitive than the current one. The uncertainty is expected to be much lower and the region where pure water has the lowest absorption can be re-explored.

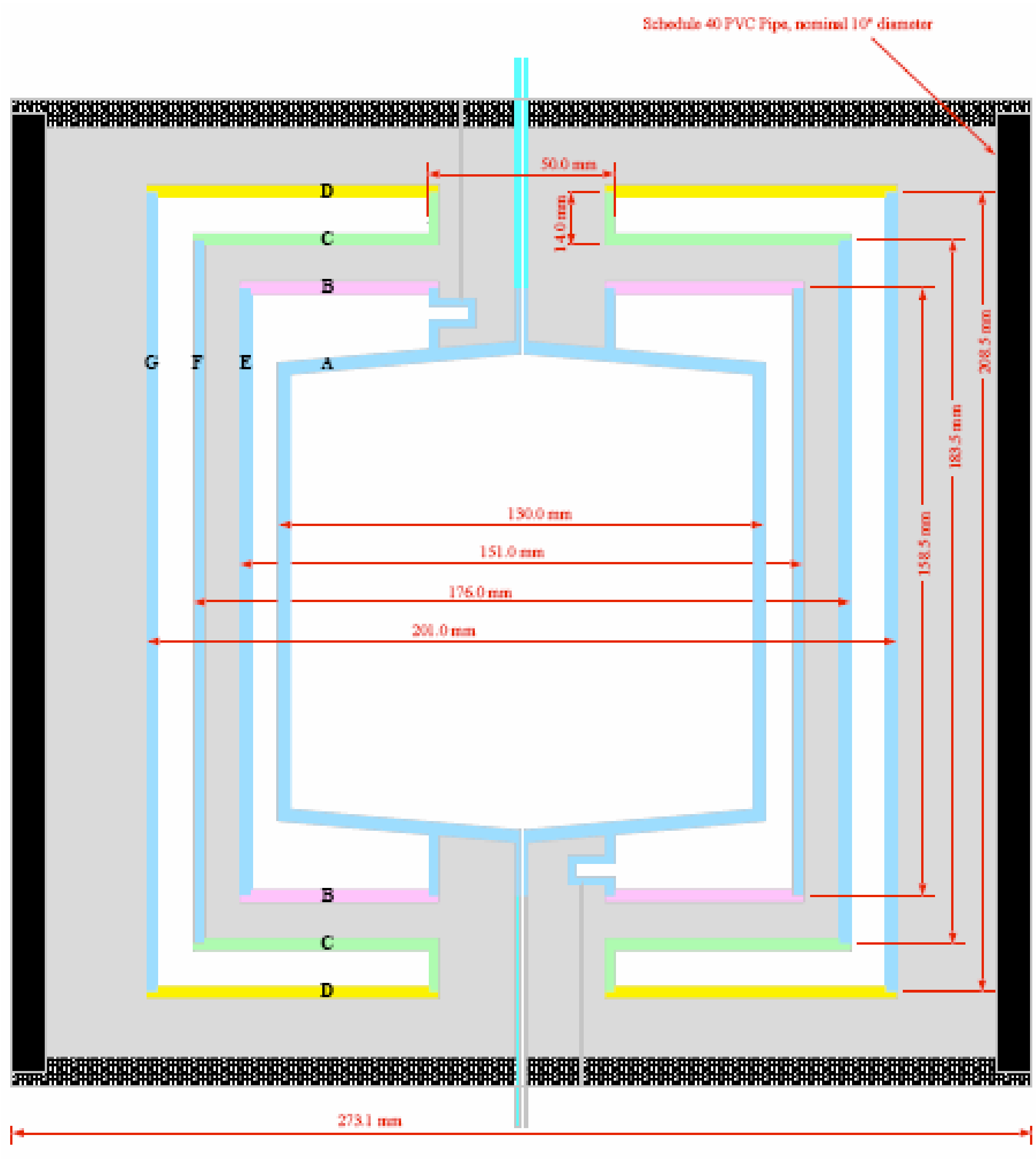

Fig. 6.10. The new ICAM design. It has a larger size, a thicker inner cavity wall, and is made of all silica except the outmost wall, whose material is irrelevant.

CHAPTER VII

CONCLUSIONS

We have constructed a new ICAM with the highly reflective diffuse material, fumed silica, to measure the absorption coefficient of ultra pure water for wavelengths from 250 nm to 400 nm in 5 nm intervals. This new material has a much higher reflectivity in UV than the Spectralon which is used in the previous ICAM. It also doesn’t have problems of deterioration under exposure to UV radiation (as does Spectralon). The new reflective material can also be used in many other applications where high reflectivity is desired, e.g. the flash lamp coupling cavity in lasers and the integrating cavity for photometric uses. The only disadvantage of fumed silica is the difficulty of fabricating it into the desired shape.

The ICAM was modified to measure the absorption coefficient of pure water in the UV region. All optical elements were optimized for UV operation. The optical collection system was optimized to favor the UV part of the light source. A new light transfer system was implemented to significantly decrease background noise so that the ICAM had a better sensitivity in the UV region where the light intensities are low. The results of the present research agree well with previous results. The robustness of the ICAM concept and its usefulness in measuring small absorption coefficient of a liquid medium has been proved. A next generation ICAM design has been proposed. It has a larger size, a thicker inner cavity wall and is made entirely of high purity silica. The sensitivity of this new ICAM is expected to be much higher. The part of the spectrum where pure water has its lowest absorption will be re-explored.

REFERENCES

1. R. Worrest, K. Wolniakowski, J. Scott, D. Brooker, and H. Van Dyke, "Sensitivity of marine phytoplankton to UV-B radiation: Impact upon a model ecosystem," Photochemistry and Photobiology **33**, 223-227 (1981).
2. S. J. D. Mora, S. Demers, and M. Vernet, *The Effects of UV Radiation in the Marine Environment* (Cambridge Univ. Press, Cambridge, 2000).
3. "Water," (2007) http://en.wikipedia.org/wiki/Water.
4. J. Tennyson, N. F. Zobov, R. Williamson, O. L. Polyansky, and P. F. Bernath, "Experimental energy levels of the water molecule," J. Phys. Chem. Ref. Data **30**(3), 735-831 (2001).
5. P. Maksyutenko, T. R. Rizzo, and O. V. Boyarkin, "A direct measurement of the dissociation energy of water," The Journal of Chemical Physics **125**, 181101 (2006).
6. P. Maksyutenko, J. S. Muenter, N. F. Zobov, S. V. Shirin, O. L. Polyansky, T. R. Rizzo, and O. V. Boyarkin, "Approaching the full set of energy levels of water," The Journal of Chemical Physics **126**, 241101 (2007).
7. M. Chaplin, "Water structure and science," (2007) http://www.lsbu.ac.uk/water/.
8. S. Prahl, "Optical absorption of water," (2007) http://omlc.ogi.edu/spectra/water/index.html.
9. A. Morel, "Optical properties of oceanic case 1 waters, revisited," Ocean Optics XIII, Proceedings of SPIE **2963**, 108 (1997).

10. A. Morel, "Optical properties of pure water and pure sea water," in *Optical Aspects of Oceanography,* N. G. Jerlov and E. S. Nielson, eds. (Academic, New York, 1974), pp. 1-24.

11. M. R. Querry, D. M. Wieliczka, and D. J. Segelstein, "Water (H2O)," in *Handbook of Optical Constants of Solids II*, E. D. Palik, ed. (Academic Press, Boston, 1991), pp. 1059-1077.

12. E. O. Hulburt, "Optics of distilled and natural water," Journal of the Optical Society of America **35**(11), 698 (1945).

13. L. H. Dawson and E. O. Hulburt, "The absorption of ultraviolet and visible light by water," Journal of the Optical Society of America **24**, 175 (1934).

14. S. A. Sullivan, "Experimental study of the absorption in distilled water, artificial sea water, and heavy water in the visible region of the spectrum," Journal of the Optical Society of America **53**(8), 962 (1963).

15. K. F. Palmer and D. Williams, "Optical properties of water in the near infrared," Journal of the Optical Society of America **64**(8), 1107 (1974).

16. M. R. Querry, P. G. Cary, and R. C. Waring, "Split-pulse laser method for measuring attenuation coefficients of transparent liquids: Application to deionized filtered water in the visible region," Applied Optics **17**(22), 3587-3592 (1978).

17. T. I. Quickenden and J. A. Irvin, "The ultraviolet absorption spectrum of liquid water," J. Chem. Phys **72**(8), 4416 (1980).

18. L. P. Boivin, W. F. Davidson, R. S. Storey, D. Sinclair, and E. D. Earle, "Determination of the attenuation coefficients of visible and ultraviolet radiation in heavy water," Applied Optics **25**(6), 877 (1986).

19. R. A. J. Litjens, T. I. Quickenden, and C. G. Freeman, "Visible and near-ultraviolet absorption spectrum of liquid water," Applied Optics **38**(7), 1216 (1999).

20. M. Hass, J. W. Davisson, H. B. Rosenstock, and J. Babiskin, "Measurement of very low absorption coefficients by laser calorimetry," Applied Optics **14**(5), 1128 (1975).

21. M. Hass and J. W. Davisson, "Absorption coefficient of pure water at 488 and 541.5 nm by adiabatic laser calorimetry," Journal of the Optical Society of America **67**(5), 622 (1977).

22. J. Stone, "Thermooptical technique for the measurement of absorption loss spectrum in liquids," Applied Optics **12**, 1828 (1973).

23. C. K. N. Patel and A. C. Tam, "Optical absorption coefficients of water," Nature **280**, 302 (1979).

24. C. K. N. Patel and A. C. Tam, "Optoacoustic spectroscopy of liquids," Applied Physics Letters **34**(7), 467 (1979).

25. A. C. Tam and C. K. N. Patel, "Optical absorptions of light and heavy water by laser optoacoustic spectroscopy," Applied Optics **18**(19), 3348-3358 (1979).

26. F. M. Sogandares and E. S. Fry, "Absorption spectrum (340–640) nm of pure water. I. Photothermal measurements," Applied Optics **36**(33), 8699-8709 (1997).
27. E. S. Fry, G. W. Kattawar, and R. M. Pope, "Integrating cavity absorption meter," Applied Optics **31**(12), 2055 (1992).
28. R. M. Pope and E. S. Fry, "Absorption spectrum (380–700 nm) of pure water. II. Integrating cavity measurements," Applied Optics **36**(33), 8710 (1997).
29. AMANDA, "Optical properties of deep ice at the South Pole: Absorption," Applied Optics **36**(18), 4168 (1997).
30. P. Elterman, "Integrating cavity spectroscopy," Applied Optics **9**(9), 2140-2142 (1970).
31. R. W. Boyd, *Radiometry and the Detection of Optical Radiation* (Wiley, New York, 1983), pp. 30-32.
32. S. Chandrasekhar, *Radiative Transfer* (Dover, New York, 1960), p. 11.
33. J. T. O. Kirk, "Modeling the performance of an integrating-cavity absorption meter: Theory and calculations for a spherical cavity," Applied Optics **34**(21), 4397 (1995).
34. E. S. Fry, J. Musser, G. W. Kattawar, and P.-W. Zhai, "Integrating cavities: Temporal response," Applied Optics **45**(36), 9053 (2006).
35. "Spectralon," (2007) http://www.labsphere.com/productdetail.aspx?id=226.
36. L. Inc., "A Guide to Reflectance Coatings and Materials," (2007) retrieved http://www.labsphere.com.

37. A. E. Stiegman, C. J. Bruegge, and A. W. Springsteen, "Ultraviolet stability and contamination analysis of Spectralon diffuse reflectance material," Optical Engineering **32**(4), 799 (1993).

38. P. C. Knee, "Investigation of the uniformity and ageing of integrating spheres," Analytica Chimica Acta **380**, 391 (1999).

39. Z. Lu, "Optical absorption of pure water in the blue and ultraviolet," (Texas A&M University, College Station, 2006).

40. J. A. Musser, "Novel instrumentation for a scattering independent measurement of the absorption coefficient of natural waters, and a new diffuse reflector for spectrscopic instrumentation and close cavity coupling," (Texas A&M University, College Station, 2006).

41. H. Barthel, M. Heinermann, M. Stintz, and B. Wessely, "Particle Sizes of Fumed Silica," Chem. Eng. Technol. **21**(9), 745 (1998).

42. R. M. Pope, "Optical absorption of pure water and sea water using the integrating cavity absorption meter," (Texas A&M University, College Station, 1993).

43. L. Cui, "Improved integrating cavity absorption meter," (Texas A&M University, College Station, 2000).

44. J. R. Taylor, *An Introduction to Error Analysis: The Study of Uncertainties in Physical Measurements*, 2nd ed. (University Science Books, Sausalito, California, 1996).

VITA

Ling Wang was born in Gushi, Henan, P. R. China in 1975, to Xigang Wang and Tianhui Huang. He earned a Bachelor of Science in Physics in 1997, then a Master of Science in Physics in 1999, from Peking University, Beijing, P. R. China. He received his Ph.D. in Physics in 2008 from Texas A&M University. Mr. Wang was happily married to Deyuan Kong on May 9, 2001. They had a beautiful daughter Jessica Wang on March 8, 2003. Mr. Wang can be reached by email at l_wang75@yahoo.com.